



UPPSALA
UNIVERSITET

*Digital Comprehensive Summaries of Uppsala Dissertations
from the Faculty of Science and Technology 442*

Structure and Dynamics of Core-Excited Species

OKSANA TRAVNIKOVA



ACTA
UNIVERSITATIS
UPSALIENSIS
UPPSALA
2008

ISSN 1651-6214
ISBN 978-91-554-7223-8
urn:nbn:se:uu:diva-8904

Dissertation presented at Uppsala University to be publicly examined in Polhemsalen, Ångströmlaboratoriet, Lägerhyddsvägen 1, Uppsala, Thursday, June 5, 2008 at 10:15 for the degree of Doctor of Philosophy. The examination will be conducted in English.

Abstract

Travnikova, O. 2008. Structure and Dynamics of Core-Excited Species. Acta Universitatis Upsaliensis. *Digital Comprehensive Summaries of Uppsala Dissertations from the Faculty of Science and Technology* 442. x, 68 pp. Uppsala. ISBN 978-91-554-7223-8.

In this thesis we have performed core-electron spectroscopy studies of gas phase molecular systems starting with smaller diatomic, continuing with triatomic and extending our research to more complex polyatomic ones. We can subdivide the results presented here into two categories: the first one focusing on electronic fine structure and effect of the chemical bonds on molecular core-levels and the other one dealing with nuclear dynamics induced by creation of a core hole. In our research we have mostly used synchrotron radiation based techniques such as X-ray Photoelectron (XPS), X-ray Absorption (XAS), normal and Resonant Auger (AES and RAS, respectively) and Energy-Selected Auger Electron Photolon COincidence (ES-AEPICO) spectroscopies.

We have demonstrated that resonant Auger spectroscopy can be used to aid interpretation of the features observed in XAS for Rydberg structures in the case of Cl_2 and $\text{Cl}1s^{-1}\pi^{*1}$ states of allene molecules. The combined use of high-resolution spectroscopy with *ab initio* calculations can help the interpretation of strongly overlapped spectral features and disentangle their complex profiles. This approach enabled us to determine the differences in the lifetimes for core-hole 2p sublevels of Cl_2 which are caused by the presence of the chemical bond. We have shown that contribution in terms of the Mulliken population of valence molecular orbitals is a determining factor for resonant enhancement of different final states and fragmentation patterns reached after resonant Auger decays in N_2O .

We have also performed a systematic study of the dependence of the $\text{C}1s$ resonant Auger kinetic energies on the presence of different substituents in CH_3X compounds. For the first time we have studied possible isomerization reaction induced by core excitation of acetylacetone. We could observe a new spectral feature in the resonant Auger decay spectra which we interpreted as a signature of core-excitation-induced keto-enol tautomerism.

Keywords: Synchrotron radiation, X-ray Photoelectron Spectroscopy (XPS), X-ray Absorption Spectroscopy (XAS), Resonant Auger Spectroscopy (RAS), Auger Electron Spectroscopy (AES), Energy-Selected Auger Electron PhotoIon COincidence (ES-AEPICO), core excitation, core ionization, linear free energy relationships (LFER), molecular-field splitting, substituent effects, nuclear dynamics, isomerization, Cl_2 , N_2O , methane derivatives, allene, acetylacetone

Oksana Travnikova, Department of Physics, Box 530, Uppsala University, SE-75121 Uppsala, Sweden

© Oksana Travnikova 2008

ISSN 1651-6214

ISBN 978-91-554-7223-8

urn:nbn:se:uu:diva-8904 (<http://urn.kb.se/resolve?urn=urn:nbn:se:uu:diva-8904>)

"I am among those who think that science has great beauty. A scientist in his laboratory is not only a technician: he is also a child placed before natural phenomena which impress him like a fairy tale."

Marie Curie

to my parents

List of Papers

This thesis is based on the following papers, which are referred to in the text by their Roman numerals.

Main bibliography for this thesis

- I **Disentangling the Complex Line Profiles in the Cl 2*p* Photoelectron Spectra of Cl₂**
O. Travnikova, R. F. Fink, A. Kivimäki, D. Céolin, Z. Bao and M. N. Piancastelli
Chem. Phys. Lett., **426** (2006) 452
- II **New Assignment of *L*_{2,3}*VV* Normal Auger Decay Spectrum of Cl₂ by *ab initio* Calculations**
O. Travnikova, R. F. Fink, D. Céolin, Z. Bao and M. N. Piancastelli
In manuscript
- III **A Detailed Study of Electron Decay Processes Following 2*p* Core Excitation in Cl₂**
M. N. Piancastelli, O. Travnikova, Z. Bao, D. Céolin and A. Kivimäki
In manuscript
- IV **A High-resolution Study of Resonant Auger Decay Processes in N₂O After Core Electron Excitation from Terminal Nitrogen, Central Nitrogen and Oxygen Atoms to the 3*π* LUMO**
M. N. Piancastelli, D. Céolin, O. Travnikova, Z. Bao, M. Hoshino, T. Tanaka, H. Kato, H. Tanaka, J. R. Harries, Y. Tamenori, G. Prümper, T. Lischke, X.-J. Liu and K. Ueda
J. Phys. B: At. Mol. Opt. Phys., **40** (2007) 3357
- V **Study of the Dissociation of Nitrous Oxide Following Resonant Excitation of the Nitrogen and Oxygen K-shells**
D. Céolin, O. Travnikova, Z. Bao, M. N. Piancastelli, T. Tanaka, M. Hoshino, H. Kato, H. Tanaka, J. R. Harries, Y. Tamenori, C. Prümper, T. Lischke, X. -J. Liu and K. Ueda
J. Chem. Phys., **128** (2008) 024306
- VI **A Study of Substituent Effects for Aliphatic CH₃-X Compounds by Resonant Auger Spectroscopy.**
O. Travnikova, S. Svensson, D. Céolin, Z. Bao, and M. N. Piancastelli
Submitted to Phys. Chem. Chem. Phys.

VII Core excitation and decay dynamics of allene.

D. Céolin, O. Travnikova, J. Palaudoux, J. Laksman, S. L. Sorensen, and M. N. Piancastelli

In manuscript

VIII Core-hole induced ultrafast isomerization of acetylacetone probed by resonant Auger spectroscopy.

O. Travnikova, D. Céolin, Z. Bao, T. Tanaka, H. Fukuzawa, K. Ueda, and M.N. Piancastelli

In manuscript

Reprints were made with permission from the publishers.

The following is a list of publications to which I have contributed to. They will not be covered in this thesis.

Extended bibliography

1. Electronic Structure of Core-excited and Core-ionized Methyl Oxirane

M. N. Piancastelli, T. Lischke, G. Prümper, X. J. Liu, H. Fukuzawa, M. Hoshino, T. Tanaka, H. Tanaka, J. Harries, Y. Tamenori, Z. Bao, O. Travnikova, D. Céolin and K. Ueda

J. Electron Spectrosc. Relat. Phenom., **156-158** (2007) 259

2. Electronic and Geometric Structure of Methyl Oxirane Adsorbed on Si (100) 2×1

M. N. Piancastelli, Z. Bao, F. Hennies, O. Travnikova, D. Céolin, T. Kampen and K. Horn

Appl. Surf. Sci., **254** (2007) 108

3. Detailed Theoretical and Experimental Description of Normal Auger Decay in O_2

Z. Bao, R. F. Fink, O. Travnikova, D. Céolin, S. Svensson and M. N. Piancastelli

Submitted to J. Phys. B

4. Search for Circular Dichroism Effects in Methyl Oxirane Adsorbed on Si (100)

M. N. Piancastelli, Z. Bao, O. Travnikova, T. Kampen, P. Schmidt, T. Deniozou, T. Braun and K. Horn

Submitted to Surf. Sci.

5. **The PCI Effect in the O₂ Near Threshold Molecular Normal Auger Spectra**
Z. Bao, R. F. Fink, O. Travnikova, D. Céolin, I. Hjelte, A. Kivimäki and M. N. Piancastelli
In manuscript
6. **Shape Resonance Affected Molecular Auger Post Collision Interaction (MAPCI) Effect of NO N K-edge Near Threshold Normal Auger Spectra**
Z. Bao, O. Travnikova, D. Céolin, R. F. Fink, and M. N. Piancastelli
In manuscript
7. **The Bonding of Chemisorbed Ethylene Oxide on Si (100) Surface**
F. Hennies, Z. Bao, O. Travnikova and M. N. Piancastelli
In manuscript
8. **Chemisorption of Methyl Oxirane on Si(100) 2×1 Surface Studied by NEXAFS and TD-DFT method**
Z. Bao, O. Travnikova, F. Hennies and M. N. Piancastelli
In manuscript
9. **Photoemission, NEXAFS and TD-DFT Method Study Chemisorption of Small Epoxy Molecules on Si(100) 2×1 surface: Ethylene oxide, Methyl Oxirane, cis-Dimethyl oxirane, trans-Dimethyl oxirane**
Z. Bao, O. Travnikova, F. Hennies and M. N. Piancastelli
In manuscript

Comments on My Own Participation

The papers presented in this thesis are a result of a team work, which is essential in modern experimental physics. My contribution to these works has varied. It is reflected, to some extent, in the position of my name in the author list and it always included participation in the experiments. In papers **VI** and **VIII** I was responsible for planning and performing the experiments, as well as analyzing the data, including correlation analysis. In all papers, of which I am the first author of, I was responsible for preparation and finalization of the manuscripts. In papers **VI** and **VII** I was responsible for the calculations. For papers **I**, **II** the calculations were performed not by me but I was responsible for the data treatment, including theoretical data in paper **II** and development of the multiple-curve fitting procedure in paper **I**.

Contents

List of Papers	iv
Comments on My Own Participation	vii
Contents	vii
 Part I: Conceptual Introduction	
1 Populärvetenskaplig Sammanfattning	3
2 Introduction	7
2.1 Spectroscopy or science of <i>seeing ghosts</i>	7
2.2 A glance through time	8
3 Experimental Techniques and Instrumentation	9
3.1 Synchrotron radiation	9
3.1.1 Beamlines	11
3.2 Electron Spectroscopy techniques	12
3.2.1 UPS	13
3.2.2 XPS	13
3.2.3 AES	13
3.2.4 Coincidence techniques	14
4 Electronic Structure	15
4.1 From the history of atom	15
4.2 Molecular structure	16
4.3 Molecular fine structure of core levels	18
4.3.1 Vibrational progressions	18
4.3.2 Molecular field splitting	19
4.3.3 Parity splitting	20
4.4 Electronic structure from electron spectra	21
4.4.1 Life-time broadening of core lines	21
4.4.2 Postcollision Interaction	21
4.4.3 Multiple-Curve fitting	22
5 Substituent Effects in Electron Spectroscopy: <i>part I</i>	25
5.1 Hammett equation and its extended forms	25
5.2 C1s ionization energies and substituent effects	26
6 Nuclear Dynamics in Core-Excited Systems	29
6.1 Ultrafast dissociation	30
6.2 Geometry change induced by core excitation	30
6.3 Rearrangement induced by core excitation	31
7 Results and Discussion	33
7.1 Electronic structure of Cl ₂ (Paper I–Paper III)	33

7.1.1	Cl2 <i>p</i> photoelectron spectra of Cl ₂ (Paper I)	33
7.1.2	Cl2 <i>p</i> normal Auger decay spectra of Cl ₂ (Paper II)	34
7.1.3	Resonant Auger decay spectra of Cl ₂ (Paper III)	36
7.2	Relaxation dynamics of core-excited states in N₂O	37
7.2.1	Resonant Auger decay processes in N ₂ O after core electron excitation to the 3 <i>π</i> LUMO (Paper IV)	38
7.2.2	Dissociation of N ₂ O after core electron excitation to the 3 <i>π</i> LUMO (Paper V)	40
7.3	Substituent effects in electron spectroscopy: part 2 (Paper VI)	43
7.3.1	Resonant Auger kinetic energies and substituent effects	43
7.4	Nuclear dynamics in core-excited molecules	47
7.4.1	Core excitation and decay dynamics of allene (Paper VII)	47
7.4.2	Core-hole induced isomerization of acetylacetone probed by RAS (Paper VIII)	51
8	Conclusions and Outlook	55
	Acknowledgments	57
	Appendix	59
	A Summary (in Russian)	59
	Bibliography	62

Part II: Papers I-VIII

Part I:

Conceptual Introduction

1. Populärvetenskaplig Sammanfattning

Allt vi ser, äter eller andas består av molekyler vilka i sin tur består av atomer. Atomen består av en atomkärna och elektroner som kretsar kring atomkärnan. Hela universum består av en stor blandning av atomkärnor, elektroner och atomer. Det är förunderligt att se hur de kombinerar sig i mångskiftande former. Ett av vetenskapens främsta mål är att förstå allt detta

Vad är spektroskopi?

Spektroskopi innebär att man studerar material genom att låta partiklar eller strålning falla in och sedan analysera energifördelningen av det som därefter kommer ut, i form av strålning eller partiklar. Vi ser i vår vardag olika exempel på detta. Betrakta våra ögon: Ljus träffar föremål i vår omgivning, dessa föremål reflekterar och absorberar ljus eller tom i vissa fall börjar föremålen fluorescera (det är detta som är effekten av vitmedel i tvätten). Med våra ögon energianalyserar vi ljuset - ljusets energi är nämligen omvänt proportionell dess våglängd. Vi människor uppfattar ljusvåglängder som färg.

Vi får energi från solen i form av ljus som kan analyseras i ett optiskt spektrum. Solspektrum består av olika slags strålning: infrarött ljus, synligt ljus och ultraviolett ljus. Strålningen karaktäriseras av våglängden. Ju kortare våglängd ljuset har, desto mer energi har strålningen. Infraröd strålning har en längd på 700nm, ultraviolett strålning återfinns från 100nm till 400nm (1nm = en miljarddels meter). Om vi till exempel tar en mikrovågsugn har strålningen i ugnen en våglängd av ungefär 12 cm. Denna strålning får vattenmolekylerna att röra sig, vilket vi observerar som värme.

För att slå loss en elektron som rör sig längst bort från syrekärnan i en vattenmolekyl måste vi använda elektromagnetisk strålning med kortare våglängder än ca 100nm (ultraviolett strålning). För att slå ut djupare liggande elektroner behövs mycket kortare våglängder (som således har mer energi). För att få loss de elektroner som är närmaste syreratomens kärna i en vatten molekyl krävs ett ljus med 2nm våglängd. Det svarar mot så kallad mjuk röntgenstrålning. (Se bilden)

I mitt arbete studerar jag just de elektroner som befinner sig nära atomkärnornorna. Man använder då röntgenstrålning för att få loss elektronerna. Idag producerar mycket intensiv röntgenstrålning med hjälp av en s.k. lagringsring, som är en speciell typ av elektronaccelerator. Denna röntgenstrålning kallas synkrotronljus.

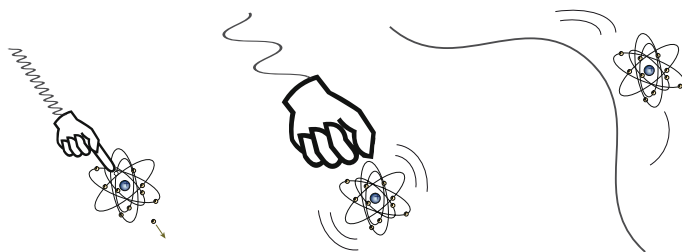


Figure 1.1: Hur elektromagnetisk strålning med olika våglängd påverkar atomer.

En synkrotron är en stor maskin, med en diameter från 30m till 800m . Elektroner accelereras till en hastighet nära ljusets i maskinen och får sedan cirkulerar runt. Eftersom elektronerna går runt är de accelererade och måste då enligt elektricitetens lagar avge elektromagnetisk strålning. Elektroner med en hastighet nära ljusets avger röntgenstrålning. Detta fenomen finns också ute i universum, till exempel i galaxen M87 som ligger på några miljoner ljusårs avstånd från vår galax.

Elektronstruktur för en biodlare

"Vad är det för likhet mellan bin och elektroner"

Atomen består av en atomkärna och elektroner som kretsar kring atomkärnan. Elektronrörelsen sker under inverkan av naturlagar. En bikupa har också sina lagar. Alla bin arbetar ihop. Deras arbetsuppgifter är väldigt noggrant fördelade. En viss sorts bin befinner sig hela tiden inne i bikupan, t.ex. bistädare och bimatrare. Andra bin kretsar runt omkring för att samla näring. I fall det dyker upp en vakans måste andra bin ersätta den tomma platsen så snart som möjligt så att kupan fungerar som en enhet.

Det är samma sak med atomer. De elektroner som befinner sig längst bort ifrån kärnan står i förbindelse med de elektroner som rör sig nära kärnan. Atomkärnan kan jämföras ramarna för honung i kupan. Ju fler ramar (protoner i atomkärnan) desto fler bin (elektroner) i bikupan (atomen). Man kan således skämtsamt kalla en elektron ett "elektronbi".

Men riktiga bin sitter inte som elektroner på en kärna. Denna består dessutom förutom av protoner (ramar) även av neutroner, som tillsammans bygger upp en atomkärna. I en elektronbikupa har varje ram bara ett "elektronbi", d.v.s. för varje proton finns bara en elektron. I en riktig bikupa finns det ungefär 2500 bin för varje ram.

Om man tar bort ett elektronbi, från en elektronbikupan, vad händer då? De andra elektronbina förstår då inte om det har blivit ett elektronbi mindre eller med antalet ramar (en proton) ökats med ett. De reagerar omedelbart i båda fall.

I mitt arbete studerar jag elektroner som befinner sig nära atomkärnan. Vi tvingar dem att lämna "elektronbikupan" (atomen) eller att bara åka iväg till bigården tillsammans med de "elektronbin" som åker runt kuporna. Vad händer då med "elektronbigården" (molekylen)? Kommer "elektronbisamhällena" att delas upp? Vem skall det utflugna biets plats? Hur det ska gå till? Och hur snabbt det ska gå? Alla sådana frågor är av intresse.

Olika bin har olika beteende på vilken bigård de befinner sig i. Några av dem stjälar honung från andras bikupor. Andra är väldigt aggressiva och skyddar sin bikupa från vilket intrång som helst. Ytterligare andra är för svaga för att skydda sin bikupa från intrånget.

Det är samma sak med atomer och atomgrupper. Ett slags atomer drar grannelektroner till sig. Andra atomer tenderar att aldrig ge ifrån sig elektroner. Ytterligare andra atomer delar helst elektroner. (Här är gård för övrigt en gräns för min liknelse: ett riktigt bi skulle aldrig ge någonting ifrån sig.) Vilken effekt får ett "elektronbi" som stannar "hemma". Detta är en fråga - som överförd till molekylernas värld - har sysselsatt mig mycket i denna avhandling.

Det krävs kunskaper för att förstå grundprinciperna för biodling. Man måste tillämpa en rad kunskaper för att få fram kvalitetshonung. Det är precis samma med forskning i atom och molekylfysik. Man måste använda vetenskapliga kunskaper för att tillverka molekyler med vissa egenskaper, modellera nya material med bättre egenskaper, utveckla nya effektivare läkemedel utan biverkningar, eller - som förra årets nobelpristagare - ta fram material med en gigantisk magnetoresistivitet. Det senare har gett oss möjlighet att minska storleken på hårddiskar kraftigt samtidigt som man har kunna öka datalagringsförmågan.

2. Introduction

2.1 Spectroscopy or science of *seeing ghosts*...

Spectroscopy refers to studying the properties of matter through its interaction with energy. A wire in the lamp bulb glows, giving off light; wood burning in the fireplace makes a chimney corner warm and lit; hot sand on the sunny beach; a rainbow in the sky; and warm food in the microwave oven - all that are evidences that matter and energy interact and how multifarious it is. Nowadays, we know that the energy given off by the matter creates a *spectrum*. The suffix ‘scopy’ arises from the Greek *σκοπειν* (=to see), hence a literal meaning of the word *Spectroscopy* is ‘*seeing a spectrum*’. It was Sir Isaac Newton who first used the word *spectrum* in his “New Theory about Light and Colors”^{*} describing the phenomenon of colored bands dispersing from white sunlight passing through a prism:

“Sir,

To perform my late promise to you, I shall without further ceremony acquaint you, that in the beginning of the Year 1666 I procured me a Triangular glass Prisme to try therewith the celebrated Phænomena of Colours. ... It was at first a very pleasing divertisement to view the vivid and intense colours produced thereby. ...

Comparing the length of this Coloured *Spectrum* with its breadth I found it about five times greater, a disproportion so extravagant that it excited me to a more then ordinary curiosity of examining from whence it might proceed. ...”

Surprisingly enough, originally the Latin word ‘*spectrum*’ was what is now called a ‘*spectre*’, *i.e.*, a phantom or apparition. You may argue with that, but, indeed, spectroscopy bears something ‘ghostly’ in the sense that it is not the matter (*e.g.* molecule) itself that we are directly looking at, but its ‘ghost’. In the end of the 17th century *spectral evidence* was testimony in Salem Witchcraft Trials that the accused witch’s spirit (*i.e.*, *spectre*) appeared to the witness in a dream. The accused were responsible for the biting, pinching and choking the witness even though they were elsewhere at the time. Well, isn’t it the *spectral evidence* we rely on to prove phenomena existing in the molecule, produced by not the molecule itself, though, but electrons or photons hitting detectors?

^{*}*Philos. Trans. R. Soc., No. 80 (19 Feb. 1671/2), 3075.*

2.2 A glance through time

“The reasonable man adapts himself to the world; the unreasonable one persists in trying to adapt the world to himself. Therefore all progress depends on the unreasonable man.”

G.B.Shaw

Looking back to those times when spectroscopy was in bud it feels odd to imagine living there without all that progress the humankind would go through later till the present day to make the study described in this work possible. Think of life without all feasible and inconceivable utilization of light, or electromagnetic radiation as physicists would call it, from the most obvious ones (like heat lamps, television, microwave ovens, cellular phones *etc.*) to the meaningful scientific applications of it which enabled countless important or useful to our lives discoveries, ranging from atomic-scale maps of proteins that have been linked to disease to insights into the riddle of high-temperature superconductivity.

One of the breakthroughs of the 20th century was the Nobel-prize winning work in the development of the spectroscopic analysis of the electromagnetic radiation with matter in the middle of the 1950s and the formulation of principles of ESCA (Electron Spectroscopy for Chemical Analysis) technique by Kai Siegbahn [1]. It had to await for about 250 years since Newton's times for X-rays to be discovered by Wilhelm Conrad Röntgen in 1895, the laws of photoelectric effect to be formulated by Albert Einstein in 1905, the Bohr model of atom to be introduced by Niels Bohr in 1913 – all Nobel-prize winning contributions to physics and fundamentals of ESCA.

Later a new source of X-rays – synchrotron radiation – opened up new horizons for spectroscopic studies of matter in biology, chemistry, material science and physics. In the 1990s synchrotron radiation based research expanded when third-generation facilities began their operation providing far more powerful X-ray beams (up to 12 orders of magnitude brighter than what was achieved with conventional X-ray tube sources!). At present there are more than 75 synchrotron radiation facilities. A number of new and very highly brilliant sources (>10) is under constructions, *e.g.* SOLEIL in France, or planned to be built in the nearest future, *e.g.* MAX IV in Sweden – a unique new synchrotron radiation facility delivering ultra-high brilliance over a very large energy range from IR to hard X-rays. Furthermore, a new type of X-ray sources, known as X-ray Free Electron Lasers (FEL), are being built. Their peak brilliance is expected to be 10 billion times brighter(!) than that of existing state-of-the-art synchrotrons [2]. There is one SASE FEL source in Hamburg – FLASH – which has already started its operation for users in summer 2005. Currently FLASH covers a wavelength range of 6.5 – 50 nm (190 – 25 eV) with gigawatt peak power and pulse durations between 10 – 50 fs. The researchers are awaiting new type of phenomena and processes at attosecond time scale to be discovered by FEL experiments. The past is fascinating, the future looks even more enthralling!

3. Experimental Techniques and Instrumentation

In this chapter the synchrotron radiation light sources used for the studies presented in this work and the experimental techniques used to carry out the measurements will be briefly described.

3.1 Synchrotron radiation

Synchrotron radiation is produced by charged particles spiraling through magnetic fields in cosmic space. It was, however, discovered in a man-made machine – synchrotron, *i.e.* cyclic particle accelerator – in 1947 as unwanted radiation which was a source for the ‘leak’ of energy of the charged particles circulating in magnetic fields inside accelerators. The first experiments utilizing synchrotron radiation were performed in ‘parasitic mode’. Unique perspectives of using this kind of radiation as a light source in various experiments caused the dedicated synchrotron radiation facilities to be constructed. The first dedicated sources of this type, classed as second-generation storage rings, use bending magnets to change the trajectory of the electrons traveling with velocities close to the speed of light. In the 90th, insertion devices, such as wigglers and undulators, which considerably increase brightness of synchrotron radiation beams, were introduced and started a new era of third-generation light sources.

A **bending magnet** causes a charged particle (*e.g.* electron) to turn and, hence, accelerate due to centripetal force applied to this particle and radiate in the tangential direction (Fig. 3.1). The bending magnet radiation is characterized by a broad energy spectrum.

A **device with a periodic magnetic structure** causes a charged particle to turn every time as it passes a magnetic pole and, hence, to experience a harmonic oscillation as it traverses the magnetic structure in the axial direction – or to experience ‘undulations’, or ‘wiggle’. It will then radiate at each turn causing the intensity of the outgoing radiation beam to be increased proportionally to the number of periods N . Such periodic magnetic

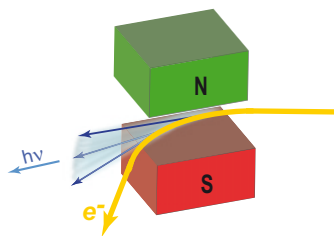


Figure 3.1: Schematic of a bending magnet radiation

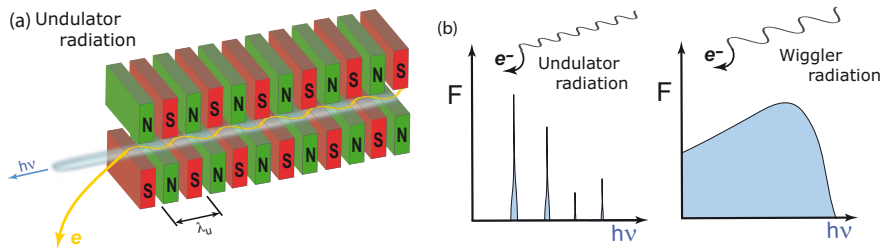


Figure 3.2: (a): Schematic of an undulator radiation; (b): comparison of photon flux for undulator and wiggler radiation as a function of photon energy

structures are linear insertion devices – undulators and wigglers – used in third-generation synchrotron radiation facilities.

Undulators are characterized by relatively weak magnetic fields which cause the amplitude of undulations to be small. Hence, the radiation is emitted in a narrow cone. Undulator radiation is characterized by harmonic radiation which is partially coherent (constructive and destructive interference occurs between wavefronts created) and peaks at certain energy values for a given magnetic field strengths (Fig. 3.2). Magnetic field strength applied to electrons circulating in a third-generation storage ring is usually controlled by the distance between the ‘sandwiched’ magnetic structures – undulator gap – which can be varied to ‘tune’ the photon energy to a desired value without drastic sacrifice in intensity of the photon flux (within certain limits, of course). ‘In-plane wiggling’ of electrons passing through the linear magnetic structure creates radiation of linear polarization for the first harmonic with zero divergence of the beam. The wavelength of undulator radiation is determined from the following equation:

$$\lambda = \frac{\lambda_u}{2\gamma^2} \left(1 + \frac{K^2}{2} + \gamma^2 \theta^2 \right)$$

$$\text{where } K \equiv \frac{eB_0\lambda_u}{2\pi mc} = 0.9337 B_0(\text{T})\lambda_u(\text{cm})$$

$$\gamma = \frac{1}{\sqrt{1 - \frac{v^2}{c^2}}} = \frac{E_e}{mc^2} = 1957 E_e(\text{GeV})$$

where B corresponds to the magnetic field strength, γ is the relativistic parameter, λ_u is an undulator period and E_e is the energy of the storage ring.

In wigglers strong magnetic fields are utilized ($K \gg 1$) which enable access to high photon energy fluxes. Due to the stronger fields the oscillation amplitude is larger and hence angular divergence of the beam is larger. Wiggler radiation is dominated by large number of harmonics which merge into continuum at high photon energies to produce radiation similar to that of a bending magnet, but with a much larger photon flux and a shift to harder x-rays [3].

3.1.1 Beamlines

A *beamline* is designed to ‘deliver’ the light to the experimental end station where measurements are performed. The beam qualities are further modified and improved while going through and passing different optical elements – such as a monochromator, which is the most important element because it ‘purifies’ the undulator set photon energy and hence strongly defines the resolution and usable photon energy range; focusing mirrors and various slits etc. A short description of the beamlines at which our experiments were carried out is given below.

Beamline I411 at MAX II, Sweden

MAX II is a third-generation storage ring of $E_e=1.56$ GeV electron energy with circumference of 90 m. The beamline I411 uses synchrotron radiation emitted by undulator with 44.5 periods (89 poles) and $\lambda_u=58.8$ mm period length which produces photon energies in the soft X-ray region of 50-1500 eV [4]. The monochromator of this beamline is a SX700 manufactured by Zeiss and consists of three optical elements: a plane mirror, a plane diffraction grating which ‘filters’ the light and a plane elliptical mirror [5]. The experimental end station is equipped with a Scienta SES-200 hemispherical electron analyzer [6] (recently changed to a Scienta R4000). The analyzer spatially disperses electrons by their kinetic energy in the electric field between the two hemispherical electrodes. Only the electrons with the trajectory matching the radius of the analyzer will pass through and hit the detector. The electron lens systems retards or accelerates the electrons to a fixed energy (*pass energy*) to obtain resolution independent of the initial kinetic energy. The electrons of the kinetic energy of about $\pm 5\%$ of the set pass energy will be detected. Therefore lower pass energies are used to achieve higher energy resolution at the expense of intensity of the signal.

Beamline 27SU at SPring-8, Japan

SPring-8 is a high-energy third-generation storage ring of $E_e=8$ GeV with circumference of 1436 m. Because of the high energy of the ring, strong magnetic fields and high K values should be used to obtain photon fluxes in the soft X-ray region. In a conventional linear undulator, higher K values result in larger intensity in high harmonics, which leads to unwanted heat load on optical elements. The beamline 27SU [7] uses a so-called *figure-8* undulator designed to deliver linear polarization with much less heat load [8]. In the figure-8 undulator, the electron moves along a special trajectory that looks like a figure of eight when projected onto the transverse plane. In order to create the figure-8 orbit, the periodic length of the outer arrays is doubled as shown in Fig. 3.3. This means that the periodic length of the figure-8 undulator is twice that of the horizontal field. The fundamental radiation generated by the horizontal field is called the 0.5th harmonic, and that one by the vertical

field is called the 1st harmonic. The beamline 27SU provides light in the range from 170 to 2800 eV.

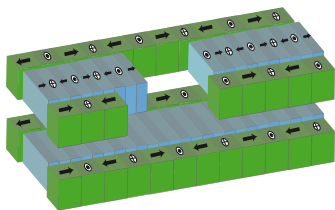


Figure 3.3: Schematic of a figure-8 undulator.

The monochromator installed on this branch is of Hettrick type [9] and provides monochromatic soft X-rays with the bandwidth ~ 50 meV in the O 1s excitation region. This high-resolution monochromator consists of three varied line space plane gratings (VLSG) and spherical focusing mirrors. The experimental end station is equipped with SES-2002 hemispherical electron energy analyzer [10].

For the coincidence experiments (Energy Selected-Auger Electron PhotoIon COincidence – ES-AEPICO) the hemispherical electron analyzer SES-2002, for which the CCD camera is replaced by a 40 mm diameter position sensitive delay line detector, is coupled with a home-made ion time-of-flight mass spectrometer ended by a position sensitive detector. After the detection of an electron a pulsed extraction field is applied in order to accelerate the ions towards a drift tube where they are separated as a function of their mass-over-charge ratio [11, 12].

3.2 Electron Spectroscopy techniques

The photoelectric effect, which is ejection of electrons through absorption of light (photons), was detected by Hertz in 1887 [13]. This phenomenon was later explained by Einstein in 1905 by invoking the quantum nature of light [14]. Einstein's photoelectric law relates the kinetic energy E_k of photoelectrons, to the frequency ν of the electromagnetic radiation and to Planck's constant h :

$$E_k = h\nu - E_b \quad (3.1)$$

where E_b is the binding energy of the electron, *i.e.* the energy that is needed to extract the electron from the material studied.

The equation (3.1) is a starting point for PhotoElectron Spectroscopy (PES) technique which is based on research performed more than 100 years.

PES techniques have developed tremendously since that time, of course, but the basic idea is the same: electrons are detected and their binding energies are deduced *via* eq. (3.1).

Some basic characteristics of different spectroscopic application are described below.

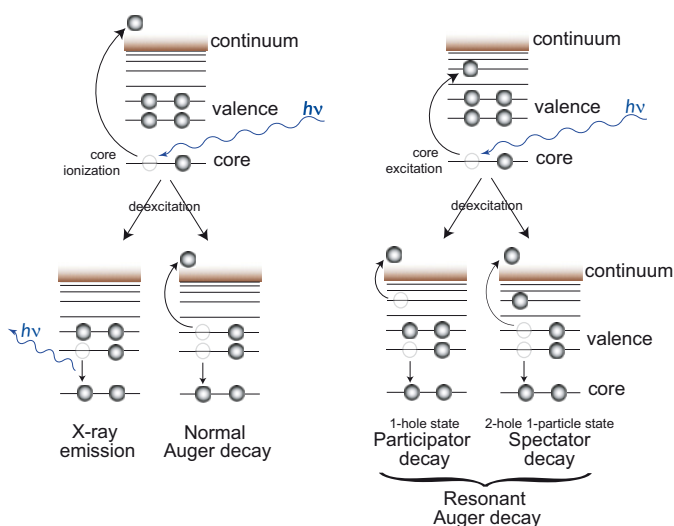


Figure 3.4: Schematic of relaxation dynamics of core-excited and core-ionized states in a classical two-step picture description

3.2.1 Ultraviolet Photoelectron Spectroscopy(UPS)

In UPS the photoelectrons removed from valence orbitals are measured. The energy of few tens of eV, which corresponds to the ultraviolet part of the electromagnetic spectrum, is sufficient to ‘kick out’ valence electrons from atomic or molecular orbitals. The valence energy level separation is small compared to core levels and is sometimes difficult to be resolved especially for polyatomic molecules. An example of UPS spectrum recorded at photon energy of 59 eV is shown in Fig. 4.2a.

3.2.2 X-ray Photoelectron Spectroscopy (XPS)

The energy of X-ray photons is already high enough to induce photoionization of deeper lying core levels. Here again the photoelectrons are detected and their kinetic energy is analyzed. The binding energies corresponding to core levels of different elements turned out to be very different [1]. Moreover the shift in binding energy is observed for an element of one type being in different chemical surroundings which makes this technique unique and powerful in studying local properties in molecules. This shift was shown to reflect the charge distribution in the molecule and may be as large as several electron volts [1] (*e.g.* in the case of the N_2O molecule the shift in binding energies of $\text{N}1s$ levels of two nitrogen atoms – terminal and central – is 4 eV).

3.2.3 Auger and Resonant Auger Electron Spectroscopy

The core-ionized states produced by photoionization are highly energetic and unstable. They eventually decay *via* radiative (fluorescence) or non-

radiative (Auger) decay releasing the energy in the form of either photon or kinetic energy of ejected electron, respectively, as schematically represented in the left panel of Fig. 3.4. The Auger decay channel is normally dominant for light elements (including C, N, O and Cl) and is considerably or almost totally quenched for heavy ones. The kinetic energy of normal Auger electrons is determined by energy difference between the energy levels involved in the Auger decay process and is therefore constant as a function of photon energy, at variance with the kinetic energy of the photoelectrons.

The tunability of synchrotron radiation sources enables the unique possibility to excite a core electron to a specific quantum state using narrow-band soft X-ray beam and to investigate the relaxation dynamics of the core-excited state in detail. It is possible only when energy of the excitation source matches exactly the energy difference between the two levels. In this case, for non-radiative (Auger) decay two pathway types can be distinguished: *participator decay*, when the electron promoted to an unoccupied valence orbital *participates* further in the process of core-hole relaxation, or it only '*spectates*' one valence electron to fill the core hole and the other to be ejected in a *spectator decay* channel as shown schematically in the right panel of Fig. 3.4. The final state produced in a participator decay channel can be also reached by photoionization of valence electrons (UPS) as it is characterized by one hole in the valence energy level.

The Auger electron ejected in the ionization continuum takes away a part of the absorbed energy. Depending on the energy left in the system after the electronic relaxation, chemical bonds can break, leading to the formation of neutral and charged species carrying the excess of energy in different forms (electronic, kinetic, and vibrational and/or rotational if the fragment is molecular).

3.2.4 Coincidence techniques

Coincidence techniques used in this work allow one to correlate the dissociation products with the decay path that leads to dissociation. These processes can be studied by detection of ions in coincidence with Auger electrons with *e.g.* a time-of-flight spectrometer which separates ions according to their mass-over-charge ratio. Selection of the internal energy of the residual ion can be performed by the kinetic energy analysis of the Auger electron and hence the fragment ions can be related to the final states reached in the electronic decay in the technique called *Energy-Selected Auger Electron Photoion COincidence* (ES-AEPICO). Using the property of core-orbital localization, the possibility of breaking bonds around the initially excited site can be investigated [15–18]. However, it usually appears that ultimately very fast energy redistribution processes scramble the dissociation channels and obscure the initially expected selectivity.

4. Electronic Structure

All things around us, no matter how different they are in size, shape, color, phase, living creatures, plants and bricks - consist only of atoms of a few dozen different types put together to form molecules which then combine to be all things we see, feel or imagine around us. And, an atom is nothing more than a number of electrons surrounding a tiny nucleus. Thus, the visible matter of the Universe is just a pile of electrons and nuclei*. It is amazing how they find the ways to organize themselves to built that vast variety of forms. One of the main goals of science is to comprehend this puzzle.

4.1 From the history of atom

The atom model which suggests that a dense, small, positively charged nucleus is surrounded by orbiting negatively charged electrons was first suggested in the beginning of the 20th century by Ernest Rutherford. For this planetary model, however, the classical electromagnetic theory would predict that an orbiting, and hence accelerating, electron would be losing energy via continuous synchrotron radiation and, therefore, would be spiraling inwards nucleus until it collapses.

In 1913 Bohr proposed that there are only certain orbits possible in the atom which have discrete quantized energies, representing energy levels. Only the size of the orbit, *i.e.* its radius, was important and it was described by n – principal quantum number. The orbits are characterized by orbital angular momentum

$$L = m_e v r = n \hbar \quad (4.1)$$

where $n = 1, 2, 3, \dots$;

r is the orbit radius; m_e is the mass of the electron and v is the velocity of the electron.

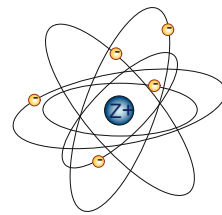


Figure 4.1: Bohr's atom

*Nuclei consist of protons and neutrons which are also composite particles. According to the Standard Model, there exist only 6 quarks (up/down, charm/strange, top/bottom), 6 leptons (electron e^- , muon μ , tau τ and neutrinos ν) and their antiparticles which interact by exchanging force carrier particles (photons, gluons, weak (W^+ , W^- , Z^0) and not yet discovered gravitons). All the visible matter in the universe is made of just the lightest fundamental particles (up/down quarks and electrons). 2 up and 1 down quarks constitute 1 proton, 1 up and 2 down quarks – 1 neutron.

In 1925 Schrödinger invented a completely new theory by introducing a wave equation which describes a motion of a particle and predicts the future behavior of a dynamic system. The Newton's laws of classical mechanics were replaced by Schrödinger's equation and quantum mechanics. As particle's size and mass approach macroscopic scale, the predictions of the classical and the quantum theories coincide, since an undefined path of the particle converges to a defined trajectory.

In the quantum theory model a particle is represented by a complex *wavefunction* $\Psi(\text{position, time})$ such that $\Psi^*\Psi$ is the probability of finding the particle at a given point in space at a given time. Therefore, an electron cannot be pictured as a localized particle in space but should be rather thought as negatively-charged "cloud" spread out around the nucleus, *i.e.*, a static wavefunction surrounding the nucleus. This cloud occupies certain regions in space, in which an electron is much more likely to be found. Heisenberg's uncertainty principle states that position and momentum of a quantum mechanical system can never be simultaneously measured with arbitrary high precision and there is a minimum for the product of the uncertainties of these two measurements (eq. 4.2). There is a likewise minimum product of the uncertainties of energy and time (eq. 4.3).

$$\Delta x_i \Delta p_i \geq \frac{\hbar}{2} \quad (4.2)$$

$$\Delta E \Delta t \geq \frac{\hbar}{2} \quad (4.3)$$

The kinetic and potential energies are transformed into the Hamiltonian which acts upon the wavefunction to generate the evolution of the wavefunction in time and space:

$$H\Psi = E\Psi \quad (4.4)$$

where E is energy, *i.e.* *eigenvalue*, of the state.

4.2 Molecular structure

According to the LCAO (linear combination of atomic orbitals) model, molecular orbitals (φ) are described as composite products of atomic orbitals (ϕ):

$$\varphi = \sum_r c_r \phi_r, \text{ where } c - \text{coefficient.}$$

The atomic orbitals used in this expansion constitute the *basis set* for the calculation. The optimum values of the coefficients are found by solving so-called *secular equations*

$$\sum_r |H_{rs} - ES_{rs}| = 0$$

where H_{rs} is a matrix element of the Hamiltonian and S_{rs} is a so-called overlap matrix element. These secular equations have non-trivial solutions if the determinant $\det[H_{rs} - ES_{rs}] = 0$. Since $S_{AA} = S_{BB} = 1$ and $S_{AB} = S_{BA} = S$, where S is the *overlap integral*, and $H_{AA} = H_{BB} = \alpha$ and $H_{AB} = H_{BA} = \beta$, where α is the molecular Coulomb integral and β is the resonance integral, the secular determinant becomes

$$\begin{vmatrix} \alpha - E & \beta - ES \\ \beta - ES & \alpha - E \end{vmatrix} = 0 \text{ and has the roots } E_{\pm} = \frac{\alpha \pm \beta}{1 \pm S}$$

and the corresponding values for the real coefficients are $c_A = \pm c_B = \frac{1}{\sqrt{2(1 \pm S)}}$

One of the orbitals formed this way can be thought of as a product of constructive interference of the two waves ($\phi_A + \phi_B$). It is a *bonding orbital* with lower energy (E_+), meaning that an electron put into this orbital will lower the overall energy and strengthen the bond between the two atoms, in contrast to the second orbital – a product of destructive interference ($\phi_A - \phi_B$) – which is an *antibonding orbital* with higher energy (E_-). [19]

The orbitals of homonuclear molecules can be classified according to their *parity*, i.e., their symmetry properties under inversion of electron coordinates. If under inversion the orbital remains indistinguishable from itself, it possesses *gerade* (or ‘even’) symmetry and is denoted as *g*. If the orbital becomes the negative of itself under inversion, it is classified as *ungerade* (or ‘odd’) and is denoted as *u*.

If z -axis is the internuclear axis, s -, p_z - and d_{z^2} -orbitals have symmetry Σ and may contribute to σ -orbitals, while p_x -, p_y - and d_{yz} -, d_{zx} -orbitals have Π symmetry and may contribute to π -orbitals. Each orbital of a particular symmetry is numbered sequentially in order of increasing energy – e.g. $1\sigma_g^2 2\sigma_u^2 3\sigma_g^2 1\pi_u^4$ and so on.

As an example which we will dwell upon in this thesis we may consider the chlorine np ($n=2,3$) orbitals $\varphi_{np, \text{sym}, p}$ with the symmetry *sym* and the parity *p* which are constructed from the atomic np orbitals at the atom I , $\phi_{np_{m_I}, I}$, by

$$\begin{aligned} \varphi_{np, \sigma, g} &= \frac{1}{\sqrt{2(1+S_{\sigma})}} (\phi_{np_{0,1}} + \phi_{np_{0,2}}), & \varphi_{np, \pi^{\pm}, u} &= \frac{1}{\sqrt{2(1+S_{\pi})}} (\phi_{np_{\pm 1,1}} + \phi_{np_{\pm 1,2}}), \\ \varphi_{np, \sigma, u} &= \frac{1}{\sqrt{2(1-S_{\sigma})}} (\phi_{np_{0,1}} - \phi_{np_{0,2}}), & \varphi_{np, \pi^{\pm}, g} &= \frac{1}{\sqrt{2(1-S_{\pi})}} (\phi_{np_{\pm 1,1}} - \phi_{np_{\pm 1,2}}). \end{aligned}$$

The overlap integral (S_{σ}, S_{π}) will be very small for Cl $2p$ core orbitals. Therefore, their contribution to the bonding of 2 chlorine atoms is negligible and they are rather localized on the atoms retaining atomic character. In contrast, overlap of the valence $3p$ orbitals will define the bond formation. The energy level scheme for molecular orbitals of Cl_2 is shown in Fig. 4.2a.

The Born-Oppenheimer approximation is most often used in molecular quantum mechanics calculations. In this approximation the electrons’ response to nuclei’s movement is extremely fast, and hence it allows one to solve the Schrödinger equation for electrons in the static electric potential arising from nuclei in different arrangement. Consequently, for different

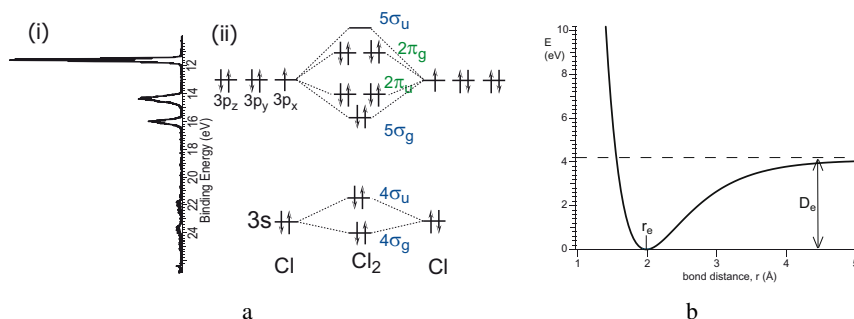


Figure 4.2: a: (i) photoelectron valence spectrum and (ii) molecular orbital energy level diagram for the Cl₂ molecule. b: Potential energy curve for the ¹Σ_g⁺ state of Cl₂

internuclear distances the energies can be obtained and potential energy curves (for diatomic molecules) or surfaces (for polyatomic species) can be constructed. The potential energy curve will have a minimum corresponding to the equilibrium conformation as shown in Fig. 4.2b.

4.3 Molecular fine structure of core levels

In this section the molecular core levels, which are the kernel of the present study, are discussed. As was mentioned above, the core orbitals of molecules, in contrast to delocalized valence orbitals, retain rather atomic character but are slightly influenced by the presence of chemical bonds and a bit different electrostatic potential from valence electrons. In most cases the largest contribution to the molecular fine structure of an electronic *p*, *d*, *f* sub-level arises from spin-orbit interaction.

4.3.1 Vibrational progressions

It had been observed long ago that the ionization from bonding molecular orbitals often leads to long vibrational progressions if the orbital is strongly bonding or angle determining. The discovery of fine structure in the core photoelectron lines was enabled due to developments of the ESCA instrumentation and considerable improvements in the resolution of the recorded spectra in the early seventies. Then, for the first time, it was possible to partially resolve vibrational structure of Cl 1s line in methane by using X-rays monochromatized in a fine focusing scheme [20]. It became apparent that core ionization is likely to result in vibrational excitations due to possibly significant differences in the potential energy curves of the ground and excited states. Thus, previous believes that photoionization of core electrons should not be accompanied by vibrational excitations because of the non-bonding character of the core orbitals were abandoned. Nowadays, instrumental resolution of the probing X-ray beam can go beyond the natural life-time broadening of the core lines. The latter will then be a limiting factor for the overall resolution. The spectra can be studied in great details. In one of the most recent vibrational

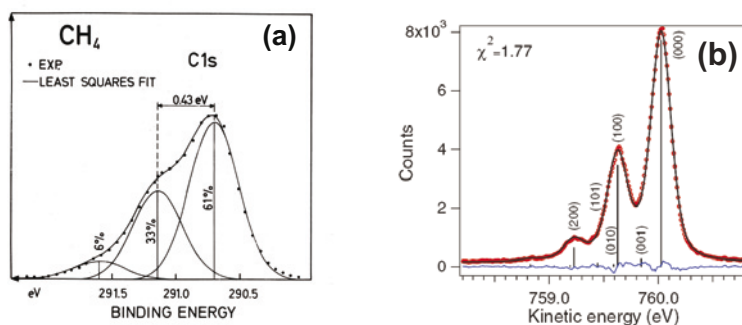


Figure 4.3: C1s photoelectron spectra of methane recorded (a): in 1974 with ESCA instrumentation [20] (Reprinted with permission from Elsevier) and (b): in 2005 at excitation energy of 1050 eV at SPring-8 synchrotron radiation facility [21] (Reprinted with permission from APS)

studies of core lines of methane, antisymmetric stretching and bending vibrational components are observed as additional peaks between the individual symmetric stretching components in the state-of-the-art photoelectron spectra (Fig. 4.3). These peaks appear due to a recoil effect of the high-energy photoelectron emission and serve as evidence for the violation of the Franck-Condon principle [21].

4.3.2 Molecular field splitting

In the beginning of the nineties, the molecular field (MF) effect was observed for low binding energy I(4d) core lines of some iodine-containing molecules [22]. MF introduces small energy differences between atomically degenerate states of p , d and f levels in molecules. In 1994 the resolution provided by synchrotron radiation from an undulator source enabled to experimentally resolve the sulfur $2p_{3/2}$ core line in H_2S into its 2 components which originate from the MF effect [23]. Even before that, in 1991 [24], evidence for the MF splitting was found by different spin-orbit splitting in the photoelectron and Auger electron spectra of H_2S . In linear molecules the coupling of the MF with spin-orbit (SO) interaction leads to $^2\Pi_{3/2}$, $^2\Sigma_{1/2}^+$ and $^2\Pi_{1/2}$ states which are also designated as $2p_{\frac{3}{2},\frac{3}{2}}^{-1}$, $2p_{\frac{3}{2},\frac{1}{2}}^{-1}$, $2p_{\frac{1}{2},\frac{1}{2}}^{-1}$. Detailed theoretical studies showed that the MF split $2p_{3/2}$ core holes have different spatial orientation. As an example, – if z is the direction of the bond as shown in Fig. 4.4 – the contribution of the $2p_z^{-1}$ configuration to the $^2\Pi_{3/2}$, $^2\Sigma_{1/2}^+$ and $^2\Pi_{1/2}$ states of HCl is 0%, 63% and 37%, respectively [25], *i.e.* the major part of the core-hole density of the $^2\Sigma_{1/2}^+$ state is oriented along the H-Cl bond, in contrast to $^2\Pi_{3/2}$ which is oriented perpendicular to the bond axis. Since the $L_{2,3}VV$ Auger decay channel is preferred if it generates a valence p hole with the same orientation as the core hole [26] and the valence electron density is smaller along the z axis due to existence of the chemical bond, the $2p_{\frac{3}{2},\frac{1}{2}}^{-1}$ state appears as the longest-lived

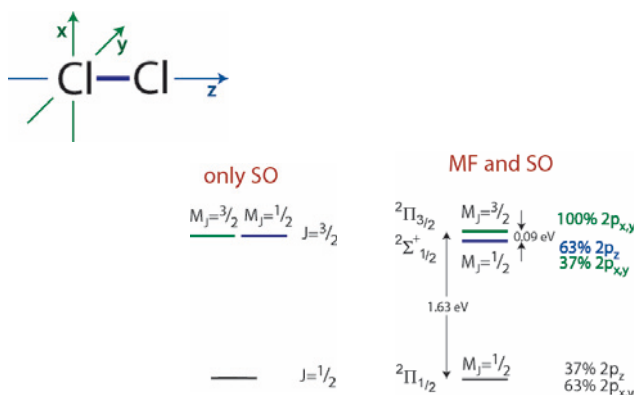


Figure 4.4: A schematic representation of the molecular field splitting in the $2p$ orbitals of the Cl_2 molecule

state, or as the one with the smallest life time width [25, 27]. Similar differences in life-time widths were observed for H_2S [28, 29] and $3d^{-1}$ states in HBr [30, 31].

4.3.3 Parity splitting

In recent years another electronic effect known as parity (gerade-ungerade) splitting has been also a subject of interest [32–36], *i.e.* the energies of minus and plus linear combinations of the $n\sigma$ or $n\pi$ orbitals on the two bound atoms may be different. A relatively large ($\sim 0.1\text{eV}$) $1\sigma_g - \sigma_u$ splitting was observed in the C_2H_2 [32, 33] and N_2 [34] molecules (see Fig. 4.5) which have triple bonds with short bond lengths. The gerade-ungerade energy splitting was shown to be mainly governed by the core-valence exchange interaction between the adjacent atoms which

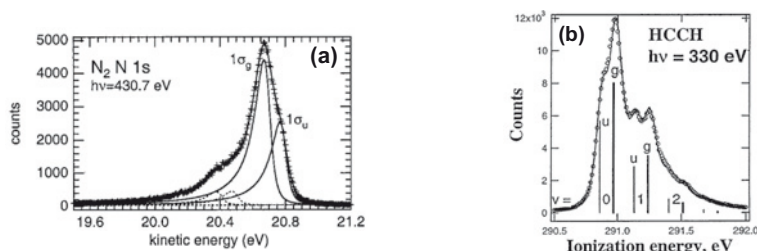


Figure 4.5: Parity splitting (a): in $\text{N } 1s$ core line of N_2 [34](Reprinted with permission from ACS) and (b): in $\text{C } 1s$ core line of acetylene [33](Reprinted with permission from APS)

do not have very tight core orbitals [35]. However, in most molecules these splittings are much too small to be resolved.

4.4 Electronic structure from electron spectra

To be able to extract important information and meaningful values for spectroscopic parameters (such as the magnitude of energy splittings, core-hole life times, vibrational spacings *etc.*) from the recorded electron spectra, the treatment of the experimental data should be performed with care. Nowadays third-generation synchrotron radiation sources allow one to record very high-resolution spectra and to observe fine structure in great detail. Nevertheless, spectral features are frequently concealed due to substantial overlap of broadened signals. Several phenomena and electronic effects are to be taken into account to make the elucidation of the spectral line shapes reliable. Some of these effects and a procedure, developed for interpretation of the experimental spectra in Paper I, are described in this section.

4.4.1 Life-time broadening of core lines

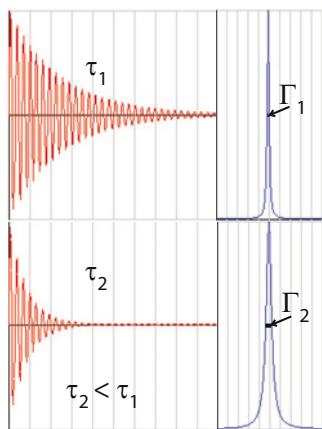


Figure 4.6: A decaying wave (left) with lifetime τ and its corresponding Lorentzian (right) with $\text{FWHM}=\Gamma$

The removal of an electron from a core-level leads to unstable core-ionized states which eventually decay either via radiative or non-radiative (*i.e.*, Auger) channel (section 3.2.3). According to the Heisenberg's uncertainty principle (eq. 4.3), the energy of the particle is less defined the shorter the lifetime is. The eq. (4.3) can be represented as $\tau\Gamma = \hbar$, where τ is the lifetime of the core-ionized state and Γ – the energy broadening of the core line, *i.e.*, the FWHM of the peak. Thus, the narrower peaks will correspond to the longer-lived core-ionized states (Fig. 4.6). The life-time broadening of exponentially decaying states is usually very well described by Lorentzian lineshapes:

$$\Lambda(E) = \frac{\Gamma}{2\pi\left(\frac{\Gamma^2}{4} + (E - E_0)^2\right)} \quad (4.5)$$

4.4.2 Postcollision Interaction

In interpretation of photoelectron and Auger spectra it is also important to take into account a so-called ‘*postcollision interaction*’, or PCI, effect. It takes place if the kinetic energy of the photoelectron emitted in the photoionization process is lower relative to the kinetic energy of the Auger electron ejected in the following non-radiative decay process. Then, at some point in the continuum of the atom, the fast Auger electron passes the photoelectron and travels further in a different potential as the screening charge it

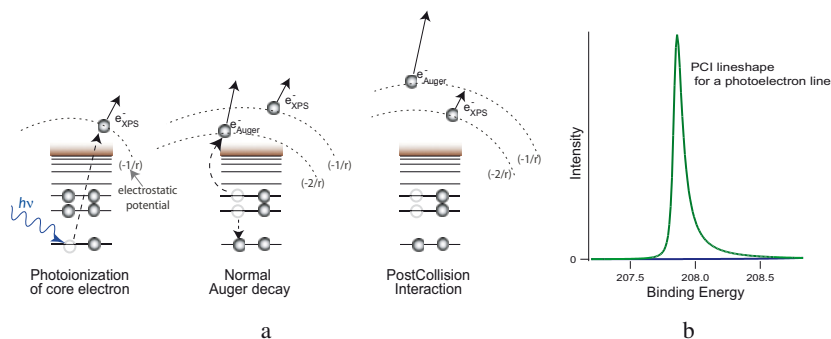


Figure 4.7: (a): Schematic for PostCollision Interaction (PCI) phenomenon and (b): PCI lineshape

feels ‘decreases’ by one unit due to the photoelectron left behind (‘retarded postcollision’). Conversely, the photoelectron feels as the charge of the nucleus has ‘increased’ and ‘slows down’ due to increased electrostatic potential (Fig. 4.7a). The decrease in kinetic energies of the photoelectron appears as a tail towards higher binding energies in XPS spectra (Fig. 4.7b). The asymmetry parameter (α) for the PCI lineshape* is derived from kinetic energies of both photoelectron (E_{XPS}) and Auger electron (E_{Auger}):

$$\alpha = \frac{1}{\sqrt{2E_{XPS}}} - \frac{1}{\sqrt{2E_{Auger}}} \quad (4.6)$$

From the equation (4.6) it is evident that the asymmetry of the core line will be larger for lower kinetic energies of photoelectron, or lower excitation energies. At some energy (‘sudden limit’) E_{XPS} is high enough that the PCI effect becomes negligible and the lineshape of the core line can be treated as being ‘PCI free’.

4.4.3 Multiple-Curve fitting

To extract meaningful information from experimental spectra, the least-squares fitting is often employed in the data treatment. Then the peaks of various lineshapes, widths and intensities can be fitted to the experimental data sets. If the lines are well resolved the direct fitting of energies and intensities of peaks is straightforward. It might be, however, rather complicated for the cases where the peaks are substantially overlapped as, *e.g.*, in the case of Cl $2p$ photoelectron spectra of Cl_2 . One can in such situations rely on theoretical support (*e.g.* *ab initio* calculations can provide values for some spectroscopic parameters; application of fundamental laws of physics (*a*) to linking and/or fixing different parameters, hence, considerably reducing the number of fitting parameters, (*b*) in such way that fit parameters of multiple-curve fits are

*PCI profile applies to Auger electron lineshapes. The photoelectron lines can be well but not precisely described by the same PCI lineshape ‘mirrored’ along the energy axis.

directly related to the underlying physical effects). An example of a possible fitting procedure, developed for interpretation of Cl $2p$ photoelectron spectra of Cl₂ (Paper I), is described below.

This fitting procedure in our studies is based on E.Kukk's fitting macro package Spectral Analysis by Curve Fitting (SPANCF) [37] designed for Igor Pro. The curve-fitting routine generates Morse potentials (eq. 4.8) on the basis of spectroscopic parameters for the ground and core-ionized states, and calculates the vibrational wavefunctions with the discrete variable representation (DVR) algorithm of Colbert and Miller [38] in order to obtain the Franck-Condon factors. The Morse potential is calculated between the bond distances from r_{min} to r_{max} with intervals:

$$\Delta x = (r_{max} - r_{min}) / n_{points}, \quad (4.7)$$

where r_{min} , r_{max} , and the number of points (n_{points}) are set to minimal values which are tested to give accurate results. The choice of smaller values is crucial as it considerably reduces the calculation and, hence, the fitting time.

$$V(r) = T_e + D_e \left(1 - \exp \left(-\sqrt{\mu/2D_e}(r - r_e) \right) \right)^2 \quad (4.8)$$

$$\text{where dissociation energy } D_e = \frac{\omega_e^2}{4\omega_e x_e} \quad (4.9)$$

where T_e is the term energy, μ is the reduced mass, r_e – the equilibrium bond distance, ω_e – the vibrational frequency for the equilibrium geometry and $\omega_e x_e$ is the anharmonicity parameter.

The vibrational energy levels (T_v with $v = 1, 2, \dots$) are derived from eq. (4.10):

$$T_v = T_e + \left(v + \frac{1}{2} \right) \omega_e - \left(v + \frac{1}{2} \right)^2 \omega_e x_e \quad (4.10)$$

According to [38] the Hamiltonian matrix for the ground and core-ionized states can be represented in the form of eq. (4.11) for the diagonal elements (H_{ii}) and eq. (4.12) for the rest of the elements (H_{ij}) of the matrix. The diagonalization of the Hamiltonian gives eigenvalues and eigenvectors (wavefunctions) for eigenstates. The squared product of multiplication of the two corresponding matrixes of eigenvectors for the ground and excited state represents Franck-Condon overlap integrals which provide intensity ratios of vibrational states (Fig. 4.8).

$$H_{ii} = \frac{\hbar^2}{\mu \Delta x^2} \cdot \frac{\pi^2}{6} + V(r) \quad (4.11)$$

$$H_{ij} = \frac{\hbar^2 (-1)^{(i-j)}}{\mu \Delta x^2} \cdot \frac{1}{(i-j)^2} \quad (4.12)$$

where $V(r)$ is derived from eq. (4.8) and Δx is the grid spacing from eq. (4.7).

The post-collision interaction (PCI) effect is taken into account when calculating individual line shapes which are then summed and convoluted with a Gaussian instrumental function. The theory of van der Straten *et al.* is used to represent the PCI effects [39]. The fitting routine enables one to fix or link different parameters and employs the Levenberg-Marquardt optimization algorithm.

Such procedure allows one to fit substantially overlapped vibrational progressions for at least two unresolved states as shown in Fig. 7.2.

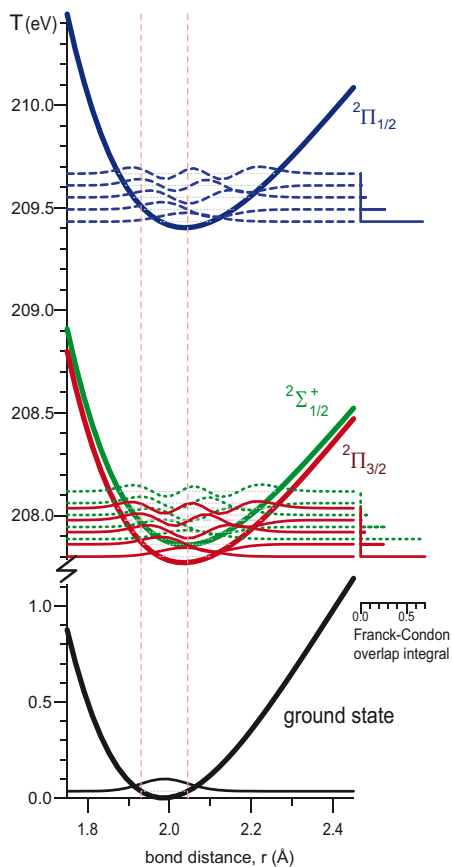


Figure 4.8: Morse potential curves, wavefunctions and Franck-Condon overlap integrals of the ground $^1\Sigma_g^+$ and $2p^{-1}$ core-ionized states of Cl₂ generated by the curve-fitting procedure [Paper I]

5. Substituent Effects in Electron Spectroscopy: *part 1*

“You may be interested to know that global warming, earthquakes, hurricanes, and other natural disasters are a direct effect of the shrinking numbers of Pirates since the 1800s.”

Bobby Henderson

5.1 Hammett equation and its extended forms

Hammett-type relationships (or linear free-energy relationships) have been extensively studied and widely used for more than 60 years. Despite their simplicity, they have been shown to be capable of predicting a vast number of chemical and physical properties of various classes of organic compounds (*e.g.* bond length, dipole moment, vibrational frequencies, reaction rate, basicity and acidity *etc* [40–42]). Hammett equation was a precursor for QSAR (quantitative structure-activity relationships) utilized in medicinal research pertaining to drug design. Linear free energy relationships are frequently used in applied chemistry for tuning of desired properties in molecules. One has observed correlations between Hammett constants and spectroscopic data from Nuclear Magnetic Resonance (NMR) shifts [43] and with Ultraviolet Photoelectron Spectroscopy (UPS) data [44].

The kernel of Hammett equation (5.1) and its extended forms is that within one series of compounds (X-Y, where X is a variable substituent and Y is a so-called reaction center) the ratio for reactivity (or any other property) of substituted and unsubstituted compound can be described in terms of the parameter σ_X , called the substituent constant.

$$\log \frac{k}{k_0} = \rho \sigma_X \quad (5.1)$$

where k_0 is the reference reaction rate of the unsubstituted reactant and k is that of a substituted reactant, ρ is proportionality, or sensitivity constant.

This constant σ_X is related to the electronic nature of the substituent X. Hammett constants are suitable for aromatic systems, such as benzene and its derivatives. Taft [45] separated these constants into two terms. One of these components (σ_I , or σ_F) represents inductive or field-inductive effects (*i.e.* through-bond and/or through-space transmission of charge in a molecule caused by electrostatic induction [46]) and the other component (σ_R , or $\sigma_{R\pm}$)

represents mesomeric, or resonance effects (*i.e.* the delocalization of electron density caused by p- or π -orbital overlap). In contrast to $\sigma_{R(R\pm)}S$, $\sigma_{I(F)}S$ are independent of the charge induced on Y by chemical or physical transformation. Correlation analysis, where resonance and inductive effects are treated separately, can be applied to systems other than benzenes with no or different resonance effects, including saturated (*i.e.* aliphatic) compounds.

Later Taft and Topsom [47] developed a more extensive parametrization which accounted for the influence of inductive effects, polarizability and resonance. The dependence of substituent effects on electronegativity was also investigated [48]. In general, an arbitrary experimental quantity y can be approximated by eq.(5.2), where σ_I , σ_R , σ_α and σ_χ are inductive (or field-inductive), resonance, polarizability and electronegativity constants respectively, ρ s are proportionality constants, y^0 corresponds to the unsubstituted compound and ϵ is the fitting error [49]:

$$y = y^0 + \rho_I\sigma_I + \rho_R\sigma_R + \rho_\alpha\sigma_\alpha + \rho_\chi\sigma_\chi + \epsilon \quad (5.2)$$

Not all the terms of the eq.(5.2) need to be statistically significant to describe different properties in various series. Polarizability is particularly important to describe substituent effects of alkyl groups while its role often turns out to be minute or even statistically insignificant for polar groups. It is even recommended to treat alkyl and polar substituents separately due to different magnitudes of their substituent effects [50].

5.2 C1s ionization energies and substituent effects

Sensitivity of binding energies for core levels toward substituent effects makes core-electron spectroscopies unique and very efficient in determining differences in chemical surroundings of atoms and distinguishing between various chemical states of compounds. In 1976 it was observed that ESCA core electron binding energies of substituted benzenes also correlate with Hammett substituent constants [51]. It was later shown [52] that this type of relationships can be used to predict binding energies for C1s ionization of organic polymers. Hammett parameters have been successfully applied in a recent study of Myrseth *et al.* [53] to investigate the role of hyperconjugation or conjugation on C1s ionization of methylbenzenes in comparison with protonation processes.

The influence of an interplay of correlated quantities such as electronegativity, polarizability and bond length with C1s ionization energies was discussed recently by Thomas *et al.* [54]. This study was, however, restricted to halogenated methanes, leaving unclear whether the same correlations exist for substituent groups. In Paper VI we apply the concept of correlations with σ_χ constants to C1s ionization energies for an extended series of substituted methanes as a test prior investigation of their resonant Auger decay properties.

The role of inductive effect on C1s ionization energies is very important. In general, increase in electron-attractive nature of a substituent causes a shift of electron density towards this substituent, more positive partial charge on adjacent carbon atom and, hence, higher energies for C1s core levels. However, the inductive effect ($\sigma_{I(F)}$) alone is not sufficient and gives only a rough description of binding energies. As was shown before by Thomas *et al.* [54] and as confirmed by results in Paper VI, polarizability also plays an important role in determining ionization energies. It is interesting to note the significance of the polarizability term on phenomena related to core electrons for polar substituents, while its role is known to be usually very small and even negligible [50] when other properties related to valence electrons are investigated (*e.g.* reaction rates). In case of the core-hole creation, this difference can be understood as polarization of the surroundings by the core hole and consequent shrinkage of the carbon atomic orbitals towards the core hole, transfer of electrons from the ligands to the core-ionized atom, and polarization of the electrons on the substituent [54].

In case of group substituents, resonance parameters ($\sigma_{R-(R)}$) in addition to inductive ones ($\sigma_{I(F)}$) give the best description of C1s binding energies (Fig. 5.1). Since aliphatic compounds do not possess π -conjugation, we suppose that group resonance constants are just suited better than group polarizabilities to describe this kind of phenomena. It should be still rather an effect of the relaxation and screening of the core hole which induces electron density delocalization, as does also the mesomeric effect.

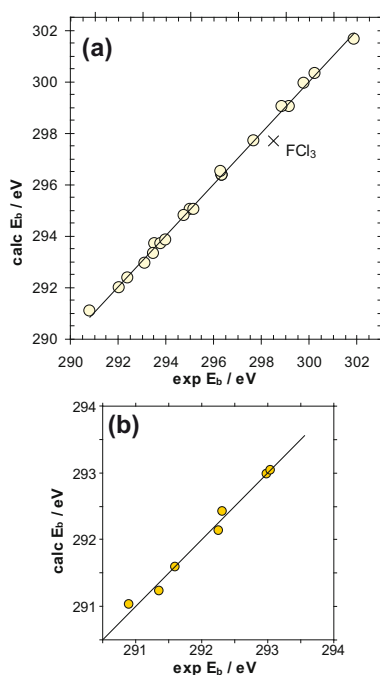


Figure 5.1: Correlation analysis of experimental C1s ionization energies of substituted methanes. (a): halogenated $CH_{4-n}Hal_n$ ($n \leq 4$) with inductive σ_F and polarizability σ_α substituent constants and (b): monosubstituted CH_3-X , where X is a group substituent, with inductive σ_F and resonance σ_{R-} constants. The straight line has a unit slope and is shown for comparison. FCl_3 -substituent is excluded from correlation.

6. Nuclear Dynamics in Core-Excited Systems

This chapter is devoted to core-excited systems. The equilibrium geometry of the core-excited states is often quite different compared to the ground state. It is common to use the so-called ‘Z+1’ approximation, or equivalent core model, to describe core-ionized or core-excited systems. In the ‘Z+1’ approximation it is assumed that the electrons close to the nucleus react to the creation of a core hole, *i.e.* relax, much less compared to the outer valence electrons. Thus the core of an atom can be treated as a point charge and in regard to the electric field felt by valence electrons, a removal of a core-electron is very similar to the addition of an extra nuclear charge. For example, the equivalent core model (‘Z+1’) for core-excited HCl* molecule is HAr, which is unstable and dissociates, or the ‘Z+1’ model for N*NO is NO₂ which is bent in the ground state in contrast to the linear ground state geometry of N₂O. Core-hole systems do not usually reach their equilibrium geometries, as the intrinsic lifetime of transient core-excited species is only of a few femtoseconds (10⁻¹⁵s). However, the phenomena attributed to nuclear motion on the same timescale as Auger decay have been observed by resonant Auger spectroscopy. Furthermore, the frequency detuning technique has been demonstrated to be a useful tool for manipulating duration time of the core-excited processes and thus giving access to different patterns in vibrational population of the final ionic states and in fragmentation [55–57]. An *effective duration time*, τ_c , is defined as

$$\tau_c = \frac{1}{\sqrt{\Gamma^2 + \Omega^2}} \quad (6.1)$$

where Γ is the core-hole lifetime width and Ω is the detuning energy defined as the difference between the excitation photon energy and the center of the vibrational envelope [58]. This means that tuning away from resonance shortens the duration time.

Possible scenarios for the nuclear dynamics are listed below and will be described in the following sections:

- *ultrafast dissociation*;
- *geometry change*, *e.g.* bending or twisting in the core-excited molecules which goes beyond Born-Oppenheimer approximation;
- *conformational changes* and possible isomerization during core excitation.

6.1 Ultrafast dissociation

The phenomenon of ultrafast dissociation was first discovered in 1986 by Morin and Nenner for the $\text{Br}3d \rightarrow \sigma^*$ excitation in the HBr molecule [59]. The dissociation involves repulsive potentials of the core-excited states.

If we promote an electron to an antibonding orbital the system will start to evolve on a dissociation pathway. It will, however, decay at some point and if the duration time of the excitation is long enough the Auger decay will happen already in a dissociated atom or a fragment so that we can observe atomic or fragment lines in the resonant Auger spectrum (Fig. 6.1).

After that discovery, ultrafast dissociation has been also observed in a number of other molecules, *e.g.* HCl [55, 60], H_2S [61, 62], H_2O [63], NH_3 [64], HF [65], O_2 [66], SF_6 [12] *etc.* where the lifetime for the $\text{F}1s$ core-hole is only about 2 fs.

The fingerprint for ultrafast dissociation is the non-dispersive behavior of the related features as a function of photon energy, *i.e.* the spectral features stay at constant kinetic energy. However, care should be taken because the non-dispersive behavior can be exhibited not only by fragment lines, but also in case the potential curves of the intermediate and of the final states are parallel, and therefore the photon energy change upon detuning causes a different group of vibrational peaks to be excited in both the excitation and the decay [67]. The way to distinguish these two decay channels is comparison of intensity of the related features for the detuned spectra relative to the ones for the spectra recorded on top of the resonance. In case of the ultrafast dissociation, the intensity has to relatively decrease in comparison to molecular features as a function of detuning from the top of the resonance, since upon detuning the time for the intermediate state to contribute to the final state spectral formation is shortened, and therefore the relative importance of the fragmentation process is reduced [68].

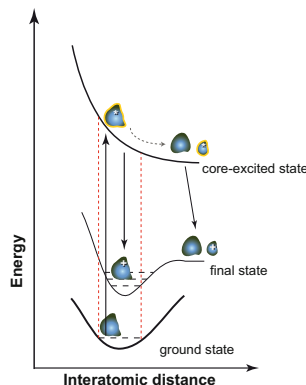


Figure 6.1: Schematic for resonant excitation to the dissociative state and consecutive Auger decay in the molecule or a core-excited fragment.

6.2 Geometry change induced by core excitation

For the molecules with degenerate lowest unoccupied π^* orbitals, excitation of a core electron to these orbitals often splits these π^* levels. For example, in the N_2O molecule as a result of the Renner-Teller splitting there are two $1s^{(-1)}\pi^{*(1)}$ states with very different equilibrium geometries, so that the lower energy state is bent while the higher energy state remains linear (Fig. 6.2).

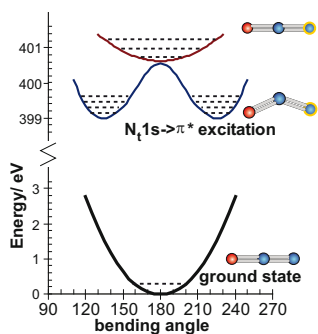


Figure 6.2: Potential energy curves for ground and $N_i 1s \rightarrow \pi^*$ core-excited states of N_2O .

Therefore, for negative detunings (lower energy side of the $1s \rightarrow \pi^*$ resonance) a bent state is mainly populated and we also see bending mode highly excited in the final state of consecutive resonant Auger decay. For positive detunings (higher energy side of the $1s \rightarrow \pi^*$ resonance) the probability would be higher to create a linear core-excited intermediate state and observe mostly stretching vibrations for the cationic final state. This effect has been observed by Miron *et al* [69].

Another example for the ultrafast geometry changes during the processes of $1s \rightarrow \pi^*$ excitations is the allene molecule which is studied in Paper VII and will be discussed later in Section 7.4.

6.3 Rearrangement induced by core excitation

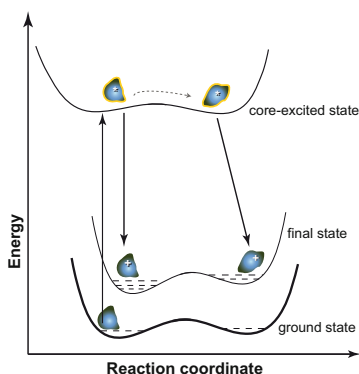


Figure 6.3: Schematic for core-hole induced isomerization.

For a system with two isomers among which one would be more stable at normal conditions, we may suppose that creation of a core hole may trigger the system to convert to its other form. Furthermore, we may be able to detect isomerization reaction by observing the electron decay spectra. However, in contrast to dissociation reactions, which involve repulsive potential energy curve of the excited state, conformational changes should proceed on a double-well potentials along the reaction coordinate for both ground and core-excited systems (Fig. 6.3). In this case, in addition to the speed of the wave packet propagation, the ability to overcome reaction barrier would be also crucial in determining whether the isomerization can be feasible in the conditions of the resonant core-electron excitations. To our knowledge, this kind of studies have not been performed so far.

To study possible core-hole induced rearrangement processes we have chosen acetylacetone system as a candidate (Paper VIII) and will discuss it later in Section 7.4.

To study possible core-hole induced rearrangement processes we have chosen acetylacetone system as a candidate (Paper VIII) and will discuss it later in Section 7.4.

7. Results and Discussion

7.1 Electronic structure of Cl₂ (Paper I–Paper III)

In Paper I we report high-resolution Cl2*p* XPS studies for the chlorine molecule for the first time. With the help of the fitting procedure described in Section 4 and *ab initio* calculations we were able to extract the values of molecular-field splitting and lifetime widths of the $2p^{-1}$ ($^2\Pi_{3/2}$, $^2\Sigma_{1/2}^{+}$ and $^2\Pi_{1/2}$) core-ionized states. The observed differences in lifetime widths are related to the underlying Auger decays from intermediate $2p^{-1}$ states which are a subject of our study in Paper II, where $L_{2,3}VV$ normal Auger decay spectrum of Cl₂ is assigned according to *ab initio* calculations performed with one-center approximation [25]. In Paper III a detailed study of the electron decay processes occurring after Cl2*p* excitation to Rydberg states in Cl₂ is discussed and a procedure to disentangle normal and resonant Auger decay contribution is presented.

7.1.1 Cl2*p* photoelectron spectra of Cl₂ (Paper I)

The Cl 2*p* photoelectron spectrum of Cl₂ shows interesting aspects as a combination of parity splitting, molecular-field splitting and spin-orbit splitting comes into play.

In the 2*p* X-ray photoelectron spectrum we can observe a shoulder for the $2p_{3/2}$ component which is due to the Molecular-Field splitting effect (Fig. 7.1). Though modern synchrotron radiation light sources allow experimentalists to record spectra with a very good resolution, the precise measurement of the MF and lifetime widths is a difficult task as they are of the same order of magnitude and the population of the molecular-field states is roughly equal. The presence of the vibrational states introduces further complications to the interpretation of the photoelectron spectra. In contrast to Cl₂, vibrational progressions in H₂S [23] and HCl [27] are rather weak. The excitation to the first vibrational level $\nu' = 1$ has only about 5% of the $\nu' = 0$ vibrational level in HCl while it is about 40%

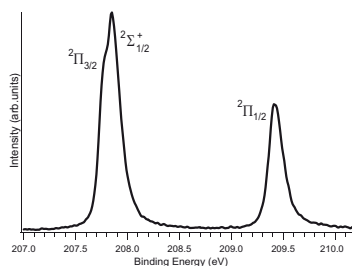


Figure 7.1: The Cl(2*p*) photoelectron spectrum recorded at a photon energy of 250eV.

in Cl_2 . This hampers to perform the fits where the energy and intensity can be obtained directly.

By applying the fitting procedure (Section 4) we were able to fit $2p$ X-ray photoelectron spectra of Cl_2 and extract spectroscopic parameters for different $2p$ core-ionized states given in Table 7.1 and one of these fits is represented in Fig. 7.2. We can see that the lifetimes are quite different for all three MF and SO split states which has been also observed in *e.g.* HCl [27] and H_2S [23]. As discussed in detail in previous works [25, 27–29, 70], the lifetimes of such states differ due to the orientational preference of the underlying $L_{2,3}VV$ Auger decay and the anisotropical electron density distribution which results from the chemical bond.

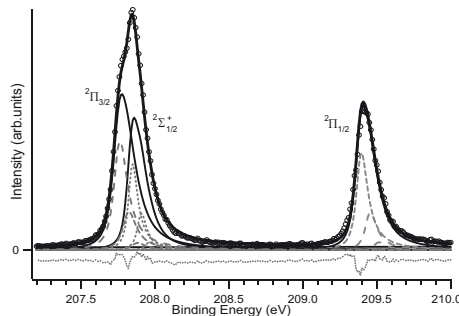


Figure 7.2: The $\text{Cl}(2p)$ photoelectron spectrum recorded at photon energy of 250 eV and pass energy of 5 eV: experimental spectrum (open circles); the final fit to the data (thick line); vibrational progressions of the $^2\Pi_{1/2}$, $^2\Sigma_{1/2}^+$ and $^2\Pi_{3/2}$ states (dashed and dotted lines); the sum of vibrational progressions for each core-hole state (thin lines); and the residue of the fit (dotted grey line below the spectrum).

Table 7.1: Experimental results for the core-ionized ($2p^{-1}$) states of Cl_2 .

state	Γ (meV)	r_e (Å)	Γ_{calc} (meV)
$\text{Cl } ^2\Pi_{3/2}$	105 ± 12	2.0346 ± 0.0021	126
$\text{Cl } ^2\Sigma_{1/2}^+$	79 ± 11	2.0389 ± 0.0014	106
$\text{Cl } ^2\Pi_{1/2}$	92 ± 5	2.0368 ± 0.0017	116
	Experiment	Theory	
Δ_{MF} (meV)	86 ± 7	86.5	
Δ_{SO} (meV) ^a	1630 ± 8	1660	
ω_e (cm^{-1})	470 ± 20	485 ^b	

^aEnergy difference between $^2\Pi_{1/2}$ and $^2\Pi_{3/2}$ states

^bAveraged over $2p^{-1}$ states

7.1.2 $\text{Cl}_2 2p$ normal Auger decay spectra of Cl_2 (Paper II)

In Fig. 7.3 a comparison of the experimental normal Auger spectrum of Cl_2 with the theoretical predictions is presented. The agreement between theory and experiment is fairly good. From the shapes of the theoretical and experimental peaks it seems that slopes of the potential energy curves are underestimated for low binding energy final states and overestimated for higher

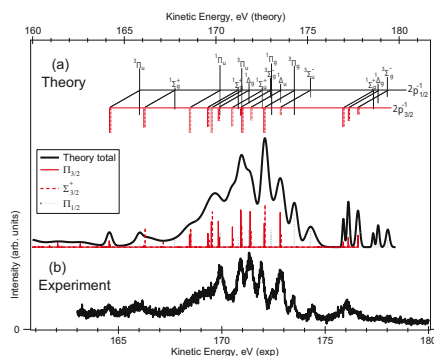


Figure 7.3: (a) Calculated total normal Auger decay spectrum of Cl₂ (solid curve and vertical bars). The vertical bars in the upper part refer to the distribution of the multiplets in the $2p_{3/2}$ and $2p_{1/2}$ series. (b) Experimental normal Auger decay spectrum recorded at 250 eV photon energy.

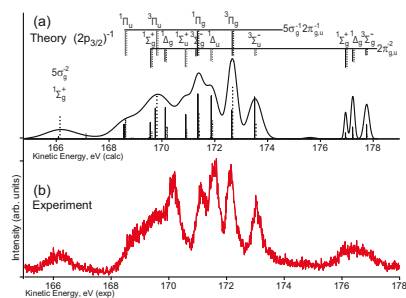


Figure 7.4: (a) Calculated electron spectrum for the normal Auger decay of the $2p_{3/2}^{-1}$ ($^2\Sigma_{1/2}^+$, $^2\Pi_{3/2}$) states of Cl₂ (solid curve and vertical bars). (b) Experimental Auger decay spectrum recorded just above $2p_{3/2}^{-1}$ and below $2p_{1/2}^{-1}$ thresholds at 208.25 eV photon energy.

binding energy states, which results in too sharp and too broad structures, respectively. However, the energy spacings for the final states are predicted rather well which enabled us to perform a reliable assignment.

Partial Auger decays from all three core-ionized states are quite different. However, the average of the two $2p_{3/2}^{-1}$ states $^2\Pi_{3/2}$ and $^2\Sigma_{1/2}^+$ is very similar to the partial Auger decay from the $2p_{1/2}^{-1}$ state.

We also recorded a decay spectrum in the photon energy region where there are no intense resonant features and where we are just above the $2p_{3/2}^{-1}$ ionization threshold but below $2p_{1/2}^{-1}$ ionization threshold (Fig. 7.4). As we can see the agreement with the theory is good.

The lowest binding energy part of the Auger decay spectrum is mainly composed of $(5\sigma_g 2\pi_{g,u})^{-2}$ final states with two holes in valence $3p$ orbitals (see

Table 7.2: The effect of the orientational preference for the orbitals involved in the Auger decay process in Cl₂. Partial Auger transition rates from the $2p^{-1}$ core-ionized states relative to transitions from $^2\Pi_{1/2}$ intermediate state.

Final-state configuration	Intermediate state		
	(0% $2p_z$) $^2\Pi_{3/2}$	(63% $2p_z$) $^2\Sigma_{1/2}^+$	(37% $2p_z$) $^2\Pi_{1/2}$
$2\pi_{g,u}^{-2}$	1.5	: 0.6	: 1.0
$5\sigma_g^{-1} 2\pi_{g,u}^{-1}$	0.8	: 1.2	: 1.0
$5\sigma_g^{-2}$	0.2	: 1.7	: 1.0

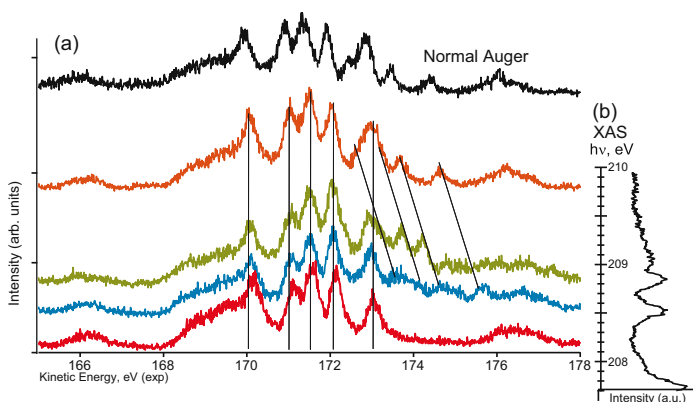


Figure 7.5: (a): experimental electron decay spectra obtained in the photon energy region above the $2p_{3/2}^{-1}$ threshold and below the $2p_{1/2}^{-1}$ threshold. The connecting lines underline the dispersion law for the different final states. A normal Auger spectrum obtained at 250 eV photon energy is shown on top for sake of comparison. (b): Corresponding absorption spectrum (XAS).

Fig. 4.2a) which accounts to 67% of the total Auger decay intensity. About half of this intensity is distributed among $(2\pi_{g,u})^{-2}$ configurations.

In Table 7.2 the relative partial Auger transition rates from the $^2\Pi_{3/2}$, $^3\Sigma_{1/2}^+$ and $^2\Pi_{1/2}$ core-ionized states to the $(5\sigma_g 2\pi_{g,u})^{-2}$ final states are summarized. We can see that for the $^2\Pi_{3/2}$ state, with the core hole oriented perpendicular to the bond axis, the probability for Auger decay decreases with increase of the number of holes created in the valence bonding $5\sigma_g$ orbital in the final state configurations, while it is reversed for the $^2\Sigma_{1/2}^+$ state which has a core hole mainly oriented along the bond axis. This indicates strong orientational preference of the orbitals involved in the Auger decay such as it generates valence p holes with the same orientation as the core hole.

Furthermore, the valence electron density along the bond axis is smaller in Cl_2 . Therefore, the probability for the $^2\Sigma_{1/2}^+$ to decay is consequently lower and it appears to be the longest-lived state with the smallest lifetime width. It is opposite for the $^2\Pi_{3/2}$ states which has the smallest contribution of the $2p_z^{-1}$ configuration.

7.1.3 Resonant Auger decay spectra of Cl_2 (Paper III)

The decay spectra following $\text{Cl}2p \rightarrow \text{Rydberg}$ excitation exhibit a rather smooth transition from resonant to normal Auger character. As shown in Paper III, it is possible to assign X-ray absorption spectra by following the similarities of decay spectra obtained after excitation to Rydberg states with the same quantum numbers. Furthermore, we can disentangle features corresponding to the decay from different spin-orbit split core-excited states by measuring Auger decay spectra in the photon energy region above threshold for the $2p_{3/2}^{-1}$ core-ionized states and below threshold for the $2p_{1/2}^{-1}$ one. Then for the spectra recorded in this region, normal Auger features stemming from

the $2p_{3/2}^{-1}$ states are showing a non-dispersive behavior while resonant Auger peaks deriving from the other $2p_{1/2}^{-1}$ one are dispersing as a function of photon energy (Fig. 7.5).

7.2 Relaxation dynamics of core-excited states in N₂O

The N₂O molecule has attracted a lot of attention due to its peculiar electronic structure, being a very simple example of a triatomic molecule with three light atoms in different chemical environments. Furthermore, the two nitrogen atoms in N₂O are not chemically equivalent. Therefore, it is possible to selectively excite core electrons from either of the nitrogen atoms and observe the differences in the decay processes. Some of the interesting properties of the two nitrogen atoms are the chemical shift between their ionization energies that one can measure in XPS (about 4 eV) [1, 71, 72], where the terminal nitrogen 1s core level exhibits a binding energy of 408.44 eV and the central nitrogen (directly bound to oxygen) has a binding energy of 412.46 eV. The energy separation in absorption measurements for transitions from either of the N 1s levels to the same intermediate state is again about 4 eV [73, 74]. Although the excitation step involving core orbitals is atomic site-selective, the decay-fragmentation processes involve valence states, and therefore one of the interesting points in studying this molecule is to verify if and to what extent the excitation from specific atomic sites affects the subsequent evolution of the system, for example in selectivity in bond breaking according to the atomic site of the primary excitation, or in selective resonant enhancement of spectral features related to the final states reached after resonant Auger decay.

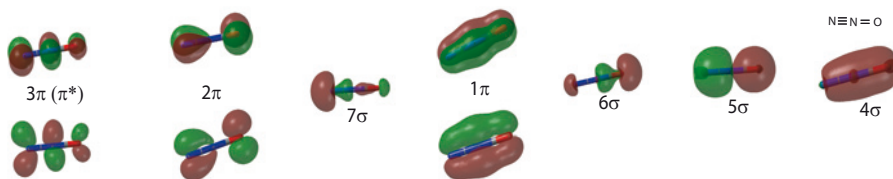


Figure 7.6: Molecular orbitals of the N₂O molecule*

N₂O has the following one-electron configuration:

$$1\sigma^2 2\sigma^2 3\sigma^2 4\sigma^2 5\sigma^2 6\sigma^2 1\pi^4 7\sigma^2 2\pi^4 3\pi^1 \Sigma^+$$

where the outer-valence orbitals (Fig. 7.6) are the 6σ level ($IE = 20.11$ eV; $6\sigma^{-1} \tilde{C}^2\Sigma^+$ state), which has mainly σ_{N-O} bonding character, the 1π level ($IE = 18.2$ eV; $1\pi^{-1} \tilde{B}^2\Pi$ state), which has a substantial contribution from the central nitrogen and partly from the oxygen atomic valence orbitals, the 7σ ($IE = 16.38$ eV; $7\sigma^{-1} \tilde{A}^2\Sigma^+$ state), which is mainly σ_{N-N} in character,

* 0.1 isosurfaces of molecular orbitals for N₂O calculated at hf/6-31g(d,p) level [this work]

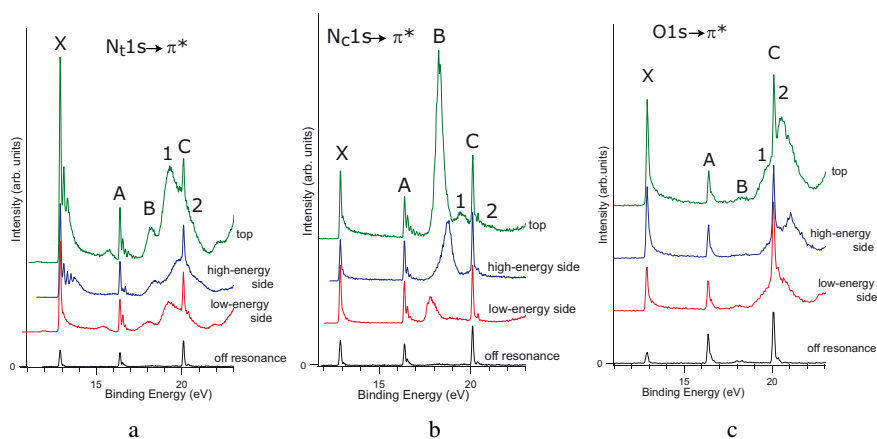


Figure 7.7: Decay spectra recorded on top, low- and high-energy sides of the resonance in the photon energy region of (a) the terminal nitrogen $N_t 1s \rightarrow \pi^*$, (b) the central nitrogen $N_c 1s \rightarrow \pi^*$ and (c) the oxygen $O 1s \rightarrow \pi^*$ transitions. The off-resonance spectra are shown for sake of comparison

and the 2π ($IE = 12.89$ eV; $2\pi^{-1} \tilde{X}^2\Pi$ state), which is mainly localized on the terminal nitrogen and oxygen atoms [75]. The lowest-lying empty molecular orbital 3π is distributed almost equally on all three atomic sites [76].

In the following discussion it will be described how these localization properties affect the resonant Auger decay [Paper IV] and how it correlates with the fragmentation patterns following core excitation measured by electron-ion coincidence techniques [Paper V]. The experiments have been carried out on the *c* branch of the soft-x-ray photochemistry beamline 27SU at SPring-8 in Japan.

7.2.1 Resonant Auger decay processes in N_2O after core electron excitation to the 3π LUMO (Paper IV)

The decay spectra of N_2O following the excitation to the $O 1s \rightarrow \pi^*$, N terminal ($N_t 1s \rightarrow \pi^*$ and N central ($N_c 1s \rightarrow \pi^*$ intermediate states are shown in Fig. 7.7 for the binding energy range 11 – 23 eV corresponding mainly to the participator decay part. In all three cases, the decay spectra were measured at three photon energies corresponding to the top of the resonant feature in the absorption curve, the low-energy side and the high-energy side (as *e.g.* shown in Fig. 7.8 for the $O 1s \rightarrow \pi^*$ excitation). The effect of detuning has been used to sample different portions of the vibrational envelope in the intermediate state and to examine how this difference reflects in the decay properties and the lineshape of the final-state spectral features.

From Fig. 7.7 we may deduce that the contribution in terms of Mulliken population of the valence molecular orbitals has a crucial role in determining the decay properties of the resonances connected to the three different core

levels. In particular, the \tilde{X} -state is resonantly enhanced mostly after excitation from the $N_t 1s$ and the $O 1s$ core levels to the π^* , while the \tilde{A} state is showing very little resonant enhancement, and the \tilde{B} state is mostly enhanced following the excitation of the $N_c 1s \rightarrow \pi^*$ intermediate state. This behavior reflects the contribution of the atomic orbitals of the three atoms to the valence electronic density: the \tilde{X} state is mostly localized on the terminal nitrogen and the oxygen atoms, while the \tilde{B} state is based mainly on the contribution from the central nitrogen atom.

The relative intensity of participator decay compared to features related to spectator decay in the $O 1s$ decay is lower than in both the N_t and N_c decay (see Paper IV). This is a general behaviour, and it is related to the depth of the core hole induced by the primary excitation: the deeper the core hole (in this case $O 1s$ versus $N 1s$), the more likely it is for the excited electron to remain in the previously empty orbital and not to participate in the decay [77].

Interestingly, in Fig. 7.7a, corresponding to the decay spectra recorded after excitation of the terminal nitrogen ($N_t 1s \rightarrow \pi^*$), in the binding energy region of the \tilde{C} state a strong resonant enhancement is observed, but it is not attributable to the \tilde{C} state, which shows some relatively small effect, but rather to another broad and partly overlapped spectral structure on which the sharp feature related to the \tilde{C} state is superimposed. This broad feature, labeled 1 in Fig. 7.7, shows a dispersive behavior which is informative on the interplay between the potential curves of the intermediate and the final states. As was mentioned in Section 6, for broad structures not attributable to ultrafast dissociation processes this behavior has been explained by the fact that the potential curves of the intermediate and of the final states are parallel. Therefore, when by changing photon energy a different group of vibrational states is selected in the intermediate state, the same group is selected in the final state, and the apparent change in binding energy is actually a change in vibrational distribution. A similar dispersive behavior is observed for the \tilde{B} final state in the decay spectra recorded after excitation of the central nitrogen ($N_c 1s \rightarrow \pi^*$) (Fig. 7.7b). Analogously, we conclude that the potential curves of the intermediate state and of the \tilde{B} final state are parallel.

Along with this behavior, another interesting point for the structure 1 observed at the two $N 1s$ decays is its binding energy position (19.59 eV). Even taking into account the apparent shift of the peak, its binding energy is lower than the binding energy of the \tilde{C} state. We attribute it to the lowest-lying state reached after spectator decay which is confirmed by *ab initio* calculations based on the SAC-CI general-R method. Usually spectator states lie at higher

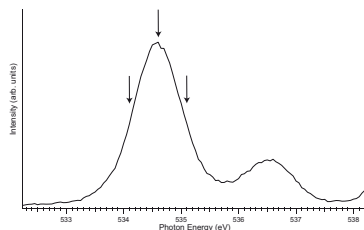


Figure 7.8: Absorption spectrum obtained in total ion yield mode below the $O 1s$ ionization threshold. The most intense lowest-lying feature corresponds to the $O 1s \rightarrow \pi^*$ transition. The arrows mark the photon energy values where decay spectra were recorded.

binding energy than participator states, but possibly in the present case we can explain the effect with a stronger than usual screening effect of the electron which remains in the state reached by the primary excitation.

The two features, labeled 1 and 2 in Fig. 7.7, are assigned as the first and the third $^2\Pi$ states with $2\pi^{-2}3\pi^1$ configuration, respectively [78]. It is interesting to observe that the two visible peaks related to spectator processes leading to $^2\Pi$ states with the same $2\pi^{-2}3\pi^1$ configuration exhibit very different relative intensities in the decay spectra following the $(N_t)1s \rightarrow \pi^*$ and the $O\ 1s \rightarrow \pi^*$ excitations. However, we cannot link the observed difference in relative intensity to a change in atomic population or a change in geometry.

7.2.2 Dissociation of N_2O after core electron excitation to the 3π LUMO (Paper V)

Analysis of the Energy-Selected Auger Electron Photoion COincidence spectra (ES-AEPICO) points to selectivity in the bond rupture depending on the final states reached in the Auger-like decay of the core holes (Fig. 7.9). This selectivity results from the different populations of these final states.

As an example, the formation of the O^+ ion is observed around 15.6 eV for the relaxation following N terminal $(N_t)1s \rightarrow \pi^*$ and at a smaller extent $O1s \rightarrow \pi^*$ excitations. It originates from predissociation of the $1^4\Sigma^-$ (see Fig. 7.10) which is coupled with \tilde{X} state by a bending coordinate [79]. Therefore, it can be correlated to the localization of doubly degenerate 2π orbitals involved in the formation of the \tilde{X} state of N_2O^+ mainly on the nitrogen terminal and oxygen atoms and by the Auger decay mechanism that is proportional to the spatial overlap of the orbitals involved in the relaxation.

For the \tilde{B} final state the N_2^+ and NO^+ ions are detected. The relaxation of the N_t and N_c $1s$ core holes leads to a more abundant production of these ions than for the $O1s^{-1}3\pi^1$ state relaxation. The \tilde{B} state can be described by the removal of an electron from the doubly degenerate 1π orbital of N_2O , which has π_{NN} and π_{NO} character. However, theoretical calculations [76, 78] have shown that the intensity of the \tilde{B} state is considerably transferred to the first shake-up state through the interaction of the $(1\pi^{-1})$ and $(2\pi^{-2}3\pi^1)$ configurations. One can consider that the participation of the 3π orbitals explains the large production of the main fragments – N_2^+ and NO^+ . These orbitals have antibonding character along the N–N and N–O bonds, which can play in favor of the formation of the $(N-NO)^+$ and $(NN-O)^+$ systems respectively. Charge localization on the NO and NN fragments is supported by the fact that the 1π orbital involved in the Auger process is concentrated around the central nitrogen atom.

For the \tilde{C} state, which is described by the removal of an electron from the 6σ valence orbital that has a σ_{NO} character, a large increase of the O^+ and N_2^+ fragments is observed at the time of the $O1s^{-1}3\pi^1$ state relaxation. This increase in the production of the ions linked to the breaking of the N–O bond is also related to the mechanism of the Auger process, i.e. explained by the overlap between the orbitals involved in the relaxation – the 6σ distributed along

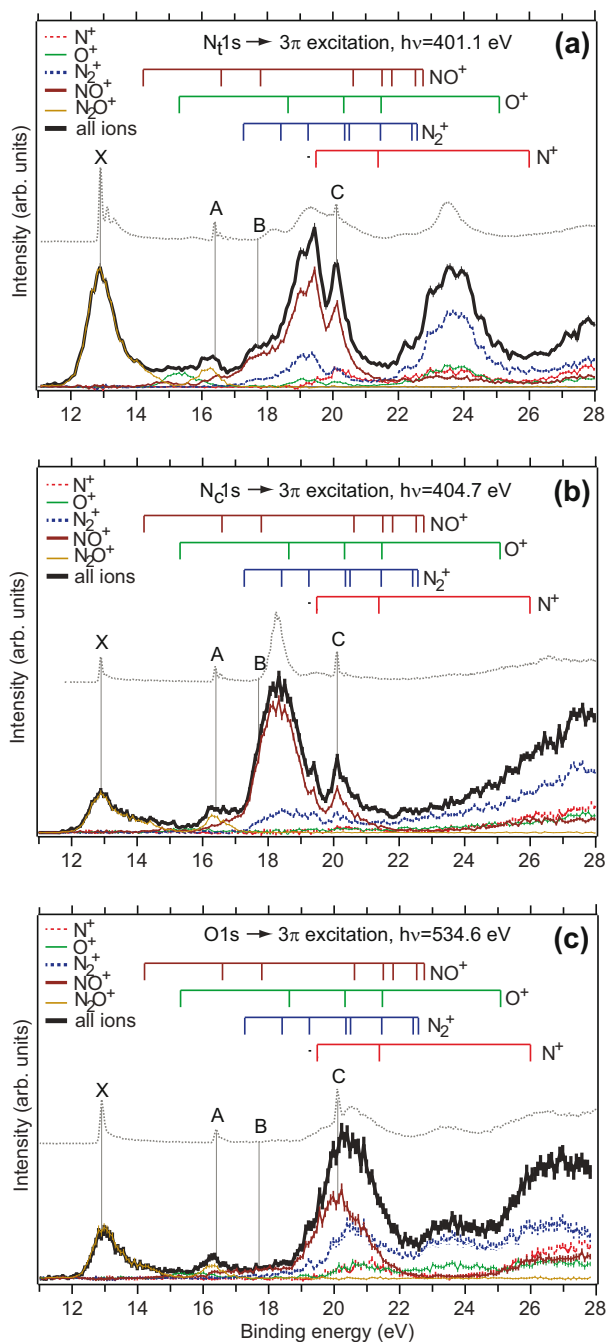


Figure 7.9: Energy-selected Auger electron/ion coincidence spectra recorded after (a) $N_f 1s^{-1} 3\pi^1$, (b) $N_c 1s^{-1} 3\pi^1$ and (c) $O 1s^{-1} 3\pi^1$ core-excited state relaxation. The distribution of the fragment intensity is given as a function of the N_2O^+ ion binding energy. The thermodynamical dissociation thresholds are shown by the colored vertical lines in the upper part of the figure.

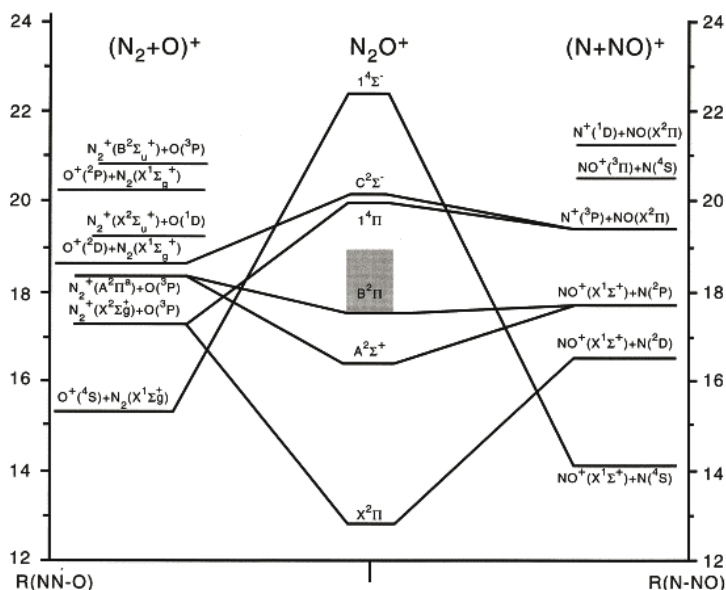


Figure 7.10: Adiabatic correlation diagram for N_2O^+ [79]. Reprinted with permission from Elsevier.

N-O, and the O1s. However, the NO^+ and N^+ ions are present especially in the high binding energy region of the \tilde{C} final state. The abundance of these ions is different for the O1s and the two N1s core-hole relaxation spectra. The explanation can be found in high-resolution resonant-Auger spectra shown on Figures 7.7a, 7.7b and 7.7c and particularly in the position of the peak attributed to the first spectator state which is located at lower binding energy than the \tilde{C} state for the relaxation of the terminal and central $N1s^{-1}3\pi^1$ states relaxation. A large contribution of the 3π orbital, *i.e.* the first unoccupied orbital, is expected to describe their electronic structure. The 3π orbital is strongly antibonding along the N-N bond and in a lesser proportion along the N-O bond. The increase in the formation of the N^+ ions and the still large amount of NO^+ ions can thus be expected for the final states reached via spectator-decay channel. Therefore, N^+ and NO^+ ions in this binding energy region are mainly due to the antibonding character of the orbitals involved in the description of the satellite states more than to the dissociation of the \tilde{C} state itself.

Another interesting point observed in ES-AEPICO spectra of N_2O is that the N_2^+ fragment is observed from 16.8 eV binding energy, which is 450 meV below the first thermodynamical dissociation limit leading to $N_2^+(^2\Sigma_g^+)+O(^3P)$ (see Fig. 7.10), consistent within our energy resolution. It is explained through avoided crossing of the potential energy surfaces related to the bent components of the \tilde{A} , \tilde{B} and $1^4\Pi$ states which results in the population of the first channel leading to N_2^+ from high vibrational energy levels of the \tilde{A} state.

7.3 Substituent effects in electron spectroscopy: part 2 (Paper VI)

7.3.1 Resonant Auger kinetic energies and substituent effects

In this study we are interested to investigate whether correlations, similar to the ones described in Section 5, can be found also for resonant Auger decay properties of core-excited systems. To our knowledge, linear free energy relationships have not been applied to RAS so far.

All the resonant Auger decay spectra following $C1s \rightarrow \sigma^*$ excitation in CH_3X series show similar pattern (Fig. 7.11). In principle we can divide them into three parts: part I with kinetic energy range up to ca 267eV, where 1-hole final states corresponding to participator decay are observed; part II ranging between 267 – ca 263eV of kinetic energy and part III starting from ca 263eV constituted from 2-hole-1-particle final states originating from spectator decay.

Noticeably, the intensity of participator decay increases with increase of electron-attractive nature of substituents. This can be understood by localization of corresponding molecular orbitals mostly on the carbon atom in case of electron-withdrawing substituents (*e.g.* NO_2), while molecular orbitals contributing to participator final states are rather diffuse over the molecule in case of electron-donating ones (*e.g.* NH_2).

In contrast to core ionization which is a rather localized process, relaxation of core-excited states involves participation of usually strongly delocalized molecular orbitals. Therefore, the observed property can not be very strictly attached to the so-called reaction center (which is $C1s$ level in this case).

As expected, in Paper VI we do not observe any significant correlations for $C1s \rightarrow \sigma^*$ excitation energies, which can be explained by diffuse nature of the unoccupied σ^* valence molecular orbitals, to which a core electron is promoted.

On the other hand, resonant Auger kinetic energies of the decay following $C1s \rightarrow \sigma^*$ excitation show very good correlation with Taft's inductive

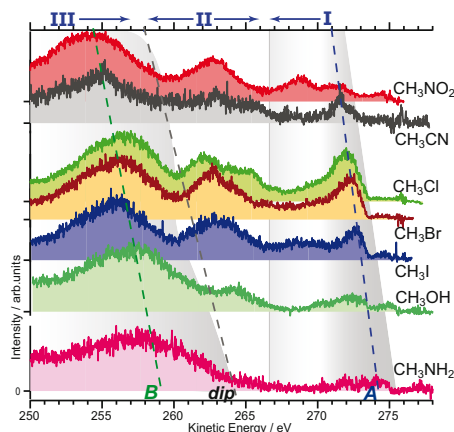


Figure 7.11: Resonant Auger decay spectra recorded on top of the $C1s \rightarrow \sigma^*$ resonance for CH_3-X ($X = NH_2, OH, I, Br, Cl, CN$ and NO_2). Contribution from direct photoemission is subtracted from all the spectra. The spectra are organized in order of increasing σ_I constants of the substituents, where amino-group has the lowest σ_I value in the series.

constants (Table 7.3). This is a bit surprising because at least two delocalized valence orbitals are involved in the process of relaxation of the core-excited states.

To understand the origin of these correlations we have drawn a schematic energy diagram to define kinetic energies (E_k) of the electrons emitted during resonant Auger decay in Fig. 7.12. Resonant Auger kinetic energy is the energy difference between the excited (E^{exc}) and the final state (E^f) (eq. 7.1). Hypothetically, we may describe this excited state by a two-step process: removal of an electron from a core level followed by addition of another electron to the corresponding unoccupied valence orbital.

If we apply the ‘Z+1’ approximation to the states with a C1s core hole, the latter addition of an electron would correspond to the electron affinity for cationic ground state of the ‘Z+1’ system ($E^{ea(Z+1)^+}$), where nitrogen would be an equivalent core atom with carbon atom missing 1 electron in the 1s electron shell (eq. 7.2). Hence the energy difference (E^Δ) between C1s $\rightarrow \sigma^*$ excited state and the C1s ionization threshold for a CH₃X molecule can be approximated to the electron affinity with the opposite sign ($-E^{ea(Z+1)^+}$) of [NH₃X]⁺. Furthermore, since the final states in resonant Auger decay process can be also reached by direct photoemission of the ground state system, their binding energies are essentially the same with the corresponding energies of valence photoelectron ionization ($E_b^{v(Z)}$). Thus we can describe resonant Auger kinetic energies by eq.(7.3):

$$E_k = E^{exc} - E^f \quad (7.1)$$

$$E^{exc} = E_b^{core} + E^{ea(Z+1)^+} \quad (7.2)$$

$$E_k = E_b^{core} - (E_b^{v(Z)} - E^{ea(Z+1)^+}) \quad (7.3)$$

Table 7.3: Correlation analysis of resonant Auger kinetic energies of CH₃-X compounds with Taft’s inductive substituent constants.

#	final state ^a	$\rho_{I,Taft}$	E^0	R	s	α	N ^b
1	\tilde{X}	-4.28(0.83)	278.21(0.37)	0.9182	0.37	0.004	7
2	A	-5.35(0.42)	274.80(0.19)	0.9849	0.19	<0.001	7
3	dip	-9.55(1.68)	264.99(0.75)	0.9309	0.75	0.002	7
4	B	-6.44(1.16)	259.29(0.52)	0.9276	0.52	0.003	7

^aEnergies for the \tilde{X} state are obtained as differences between C1s $\rightarrow \sigma^*$ excitation energies and corresponding binding energies from [76]: $E_{kin} = E_{exc} - E_b$; for the A, B states and dip – as energy positions of the peaks A, B and of the dip in the experimental spectra fitted with arbitrary asymmetric voigt functions.

^bRows from left to right: regression equation number (#); regression coefficient (ρ_I) for Taft’s inductive σ_I (standard deviation is given in parentheses); kinetic energy (E^0) of the unsubstituted compound from correlation analysis in eV (standard deviation is given in parentheses); correlation coefficient (R); standard deviation of regression (s); significance level (α); number of data points (N).

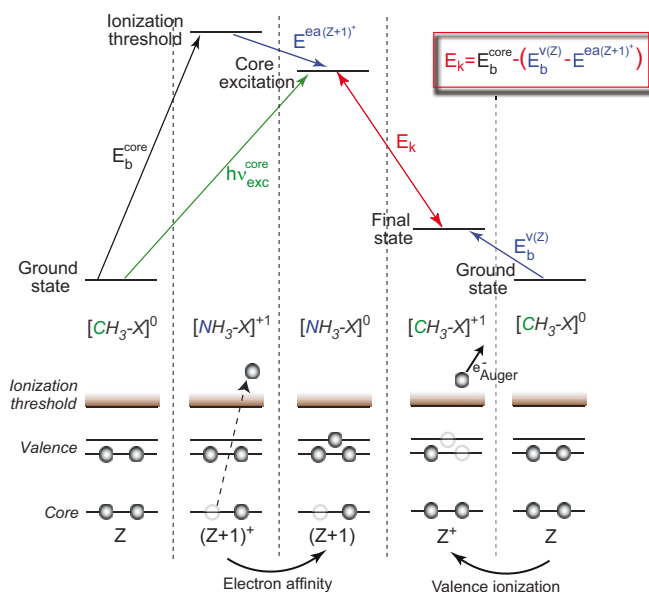


Figure 7.12: Schematic energy diagram for description of resonant Auger kinetic energies with the 'Z+1' approximation.

where E_b^{core} is the core-electron binding energy.

$(-E^{ea(Z+1)+})$ term can be qualitatively compared to valence ionization of neutral 'Z+1' system. $[NH_3X]^0$ is not stable and prefers +1 charged ionic state at normal conditions. We may expect that its valence ionization energy, as well as $(-E^{ea(Z+1)+})$, should be influenced by the ability of the substituent X to draw away undesired additional electron density from the nitrogen atom. On the contrary, the valence ionization energy ($E_b^{v(Z)}$) of the stable $[CH_3X]^0$ molecule would be affected by the power of the substituent to compensate electron density deficiency in the ionized state. Hence $E_b^{v(Z)}$ and $(-E^{ea(Z+1)+})$ should contain components describing the ability of the substituent to delocalize electron density in the opposite directions and therefore, they might become negligible in the sum $(-E^{ea(Z+1)+} + E_b^{v(Z)})$. This property should be described by σ_α and/or $\sigma_{R(R\pm)}$ constants as it reflects an adjustment of the system to the charge induced by the observed process.

This hypothesis is confirmed by regression analysis for the sum of the experimental energy distances from σ^* excitation energies to the ionization threshold (E^Δ) with $\widetilde{E}_b^{v(Z)}$ final state binding energies ($E_b^{v(Z)}$) for the investigated compounds in the CH_3X series (Fig. 7.13). Moreover, calculated values for the 1st electron affinities for $[NH_3X]^+$ agree fairly good with observed experimental E^Δ values, which supports the validity of the proposed model.

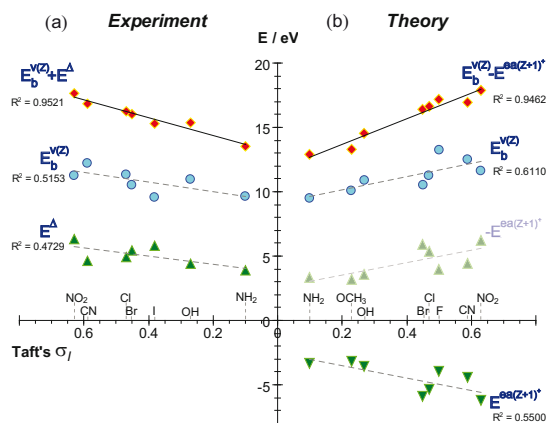


Figure 7.13: (a) Experimental $E_b^{v(Z)}$, E^Δ and (b) theoretical $E_b^{v(Z)}$, $E^{ea(Z+1)^+}$ values versus Taft's inductive constants. $E_b^{v(Z)}$ is binding energy of \tilde{X} state and E^Δ – energy distance between $\text{Cl}s \rightarrow \sigma^*$ excited state and the Cls ionization threshold for $[\text{CH}_3\text{X}]^0$, $E^{ea(Z+1)^+}$ – 1st electron affinity of $[\text{NH}_3\text{X}]^+$. The lines represent the trendlines of regression analysis and regression coefficients R^2 are shown next to the lines.

7.4 Nuclear dynamics in core-excited molecules

7.4.1 Core excitation and decay dynamics of allene (Paper VII)

Allene, or 1,2-propadiene, $\text{CH}_2=\text{C}=\text{CH}_2$, is the simplest cumulene, or compound with cumulated (consecutive) double bonds (Fig. 7.4). Its three carbon atoms subdivide in two chemically inequivalent groups, two terminal and one central carbon atoms with different chemical environment. Therefore, absorption spectra measured in a photon energy region below the $\text{C}1s$ thresholds will exhibit chemically shifted spectral features related to both groups.

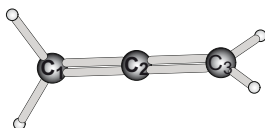


Figure 7.14: Ground state geometry of allene

The ground state of allene is described within the independent particle approximation by the electronic configuration $(1a_1)^2(1b_2)^2(2a_1)^2(3a_1)^2(2b_2)^2(4a_1)^2(3b_2)^2(1e)^4(2e)^4$. The valence orbitals have the following description: the $2e$ orbitals are mainly described by two perpendicular bonding π -type orbitals localized on $\text{C}_1=\text{C}_2$ and $\text{C}_2=\text{C}_3$ double bonds, respectively; the $1e$ orbitals are mainly localized on the $\text{C}=\text{CH}_2$ groups; the $3b_2$ orbital is delocalized over the molecule and is described by $\text{C}=\text{C}=\text{C}$ σ bonds (see Fig. 7.4). The description of the vibrational

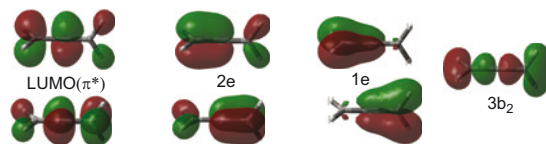


Figure 7.15: Valence molecular orbitals of allene (0.05 isosurfaces).

progressions of these states requires considerations of Jahn-Teller (JT) distortions and vibronic couplings, which lead to splittings of the structures related to the lowest valence ionized states. A deeper analysis of the vibronic structure of the \tilde{X} state, both experimental and theoretical, shows that one can well describe the corresponding progression by taking into account only two vibrational normal modes: CH_2 vs CH_2 torsional and antisymmetric $\text{C}=\text{C}$ stretching modes [80–83]. The low-energy part of the \tilde{X} band involves mostly the torsional motion, whereas at higher energy (above ~ 10 eV) this mode couples with the antisymmetric $\text{C}=\text{C}$ stretching.

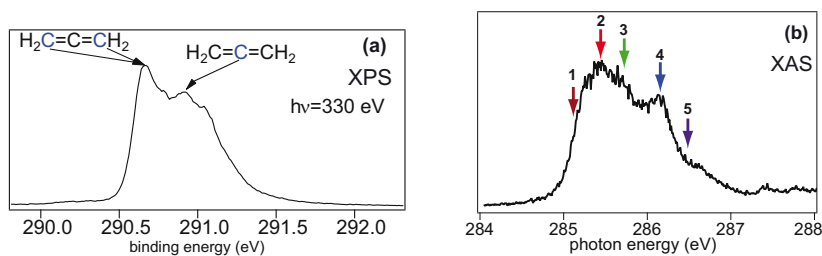


Figure 7.16: (a): $\text{C}1s$ XPS spectrum of allene recorded at 330 eV; (b) absorption spectrum of allene in the vicinity of the $\text{C}1s \rightarrow \pi^*$ resonance.

The main purpose of our work presented in Paper VII was to assign part of the structures observed in the X-ray absorption spectrum of allene at the C K-edge with the help of resonant Auger spectroscopy and analysis of the vibrational modes excited in the final states after $\text{C}1s \rightarrow \pi^*$ transition. To be able to link the photon energy with a specific transition, *i.e.* carbon terminal or central $1s$ electron to the π^* orbital, we suppose that the excitation of the terminal carbon is more likely to induce asymmetrical nuclear motion in the core-excited state by vibronic coupling, contrary to the excitation of the central carbon that is expected to induce preferentially vibration of symmetric nature.

$\text{C}1s$ X-ray photoelectron spectrum and absorption spectrum recorded in the vicinity of the $\text{C}1s \rightarrow \pi^*$ resonance are shown in Fig. 7.16 a and b. Resonant Auger decay spectra measured at the photon energies marked in Fig. 7.16b are shown in Fig. 7.17. From Fig. 7.17 we can clearly see that the maximum of the vibrational envelope corresponding to the \tilde{X} state is moving as a function of photon energy. As was described above it should indicate that antisymmetric stretching modes are more efficiently excited as we move towards higher energies, while the lowest vibrational level corresponding to the torsion motion can be reached only with negative detuning (curve 1 in Fig. 7.17). At the photon energy corresponding to a feature at higher energy side of the $\text{C}1s \rightarrow \pi^*$ structure,

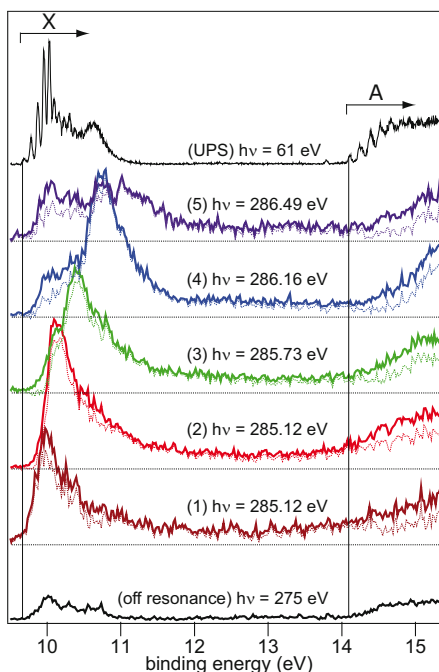


Figure 7.17: Resonant Auger decay spectra recorded after $\text{C}1s \rightarrow \pi^*$ excitation at the energies corresponding to the arrows marked in Fig. 7.16b.

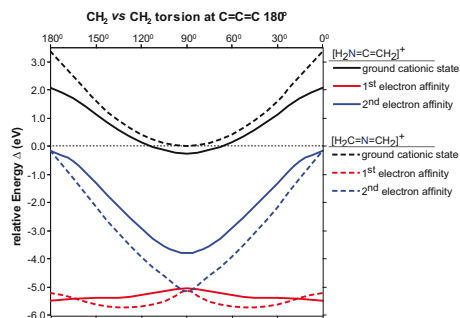


Figure 7.18: Potential energy scans for CH_2 torsion motion for core-ionized and core-excited states of allene with the “Z+1” approximation. The initial geometry is the ground state geometry of allene with torsion angle equal to 90° .

labeled 4 in Fig. 7.16b, 7.17, the population of higher vibrational modes is higher if the absorption cross-section is taken into account. Furthermore, at this energy the intensity is also increased for the $\tilde{\text{A}}$ final state, which has electron density mainly localized at CH_2 groups of allene. This suggests that the second main structure (4) should correspond to the excitation of the terminal carbon atom, which would be, however, a bit unexpected because of the reverse ordering of the core-ionized states (Fig. 7.16a).

Independently of this analysis, we have performed *ab initio* calculations in order to determine the relative energy positions of the $\text{C}_{\text{terminal}}1s$ or $\text{C}_{\text{central}}1s$ core-excited and core-ionized states. We have used the “Z+1” approximation to represent $\text{C}1s \rightarrow \pi^*$ core-excited molecules ($\text{H}_2\text{C}=\text{N}=\text{CH}_2$ and $\text{H}_2\text{N}=\text{C}=\text{CH}_2$ for $\text{C}_{\text{central}}1s \rightarrow \pi^*$ and $\text{C}_{\text{terminal}}1s \rightarrow \pi^*$ excitations, respectively). 2D rigid potential energy scans (PES) along the $\text{C}=\text{C}=\text{C}$ bending, CH_2 torsion and $\text{C}=\text{C}$ bond length coordinates have been calculated and for each PES the energies of the ground cationic state and first two electron affinities were computed at the SAC-CI(SD-R)/D95* level of theory. The same method for the description of $\text{C}1s$ core-excited states was also used in Paper VI, where it showed reasonably good agreement with experiment (Fig. 7.13). It appeared, however, necessary to adjust the relative energies for the cationic ground states corresponding to the $\text{C}_{\text{terminal}}1s$ or $\text{C}_{\text{central}}1s$ core-ionized states of allene to the experimental IP values observed for these states.*

The results of the calculations are shown in Fig. 7.18–7.19. From the scans we can see that, as described in Section 6, the $\text{C}1s \rightarrow \pi^*$ excited states are split. However, the splitting for the terminal C-atom is obviously larger, while the two $\text{C}_{\text{central}}1s^{-1}\pi^{*1}$ states remain degenerate at the ground state geometry. The origin of these uneven splittings for two inequivalent carbon atom groups could probably be found in the description of π^* orbitals (Fig. 7.4): the electron density distribution around the terminal carbon is very different for the two LUMOs, where for one of them there is a considerable lack of it.

*This energetic ordering was supported by theoretical calculations for the $\text{C}1s$ core-ionized states of allene at the B3LYP/cc-pVDZ level of theory, where the core of the ionized carbon atom was represented by an effective core potential (ECP), scaled to account for only one electron in the $1s$ shell [84]. However, a somewhat larger energy difference of 422 meV between $\text{C}_{\text{central}}1s$ and $\text{C}_{\text{terminal}}1s$ was calculated.

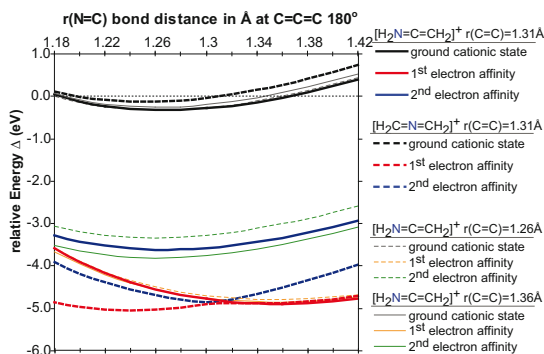


Figure 7.19: Potential energy scans for $r(\text{C}=\text{N})$ bond lengths for core-ionized and core-excited states of allene with the “Z+1” approximation at $r(\text{C}=\text{C})$ equal to 1.31 Å for $\text{H}_2\text{C}=\text{N}=\text{CH}_2$ and $r(\text{C}=\text{C})=1.31, 1.26$ and 1.36 Å for $\text{H}_2\text{N}=\text{C}=\text{CH}_2$. The initial geometry is the ground state geometry of allene with $r(\text{C}=\text{C})=1.31$ Å.

Therefore, if we assume that the $1s$ shells of the terminal carbon atoms are localized, the promotion of the $1s$ core electron to these two π^* orbitals could not be equivalent. The significance of the antisymmetric stretching mode is also supported for the higher energy state $C_{\text{terminal}}1s^{-1}\pi^{*1}$ by PES along the $r(\text{N}=\text{C})$ bond distance coordinate at different $r(\text{C}=\text{C})$ values (Fig. 7.19): the lowest energy for this state corresponds to the antisymmetric geometry of the equivalent core model system $\text{H}_2\text{N}=\text{C}=\text{CH}_2$ with $r(\text{N}=\text{C})=1.26$ Å and $r(\text{C}=\text{C})=1.36$ Å.

To conclude, we have identified two main contributions in the absorption spectrum: the one at the low energy side (below ~ 286 eV) is mainly attributed to the two $C_{\text{central}}1s^{-1}\pi^{*1}$ and the lowest $C_{\text{terminal}}1s^{-1}\pi^{*1}$ states, whereas the second structure at higher photon energy is linked to the excitation of the terminal carbon $1s$ electron.

7.4.2 Core-hole induced isomerization of acetylacetone probed by RAS (Paper VIII)

Acetylacetone (2,4-pentanedione) has been extensively studied both experimentally and theoretically due to its interesting properties. Acetylacetone (AcAc) is one of the simplest molecules which possess intramolecular hydrogen bond and a proton-tunneling exchange between the two oxygen atoms. It is known to change its functionality via keto-enol tautomerism depending on the surrounding media and temperature [85, 86].

As a free molecule, AcAc is predicted to exist in several possible stable forms, among which the asymmetric enol has the lowest energy and predominates at room temperature (Fig. 7.20) [87–91]. The equilibrium content of enol for pure acetylacetone is 81.4% in the liquid phase and 93.3% in vapor [92].

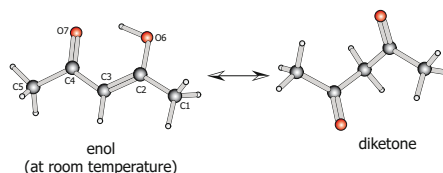


Figure 7.20: Lowest energy isomers of acetylacetone.

Observation of shifts in keto-enolic equilibrium of AcAc induced by, for example, temperature is possible by UPS due to different photoionization potentials of the valence electrons for the diketone and enol forms in the 8–11 eV energy region of the spectrum. The orbital ordering is $\pi_{C=C}(9.08\text{eV}) < n_O^-(9.63\text{eV})$ and $n_O^-(9.63\text{eV}) < n_O^+(10.16\text{eV})$ for enol and diketo-forms, respectively, where n_O^- and n_O^+ are antisymmetric and symmetric combinations of the carbonyl in-plane 2p orbitals [86]. Hence the increase in temperature leads to the growth of the peak intensity around 10.16 eV which is undetectable at room temperature (Fig. 7.21) [85, 86].

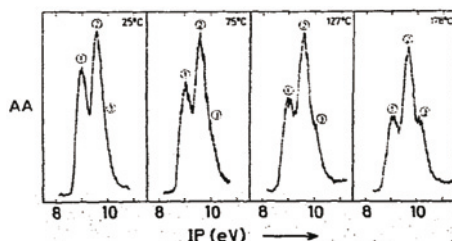


Figure 7.21: Photoelectron spectra of acetylacetone (AA) at some selected temperatures [85]. Reprinted with permission from Elsevier.

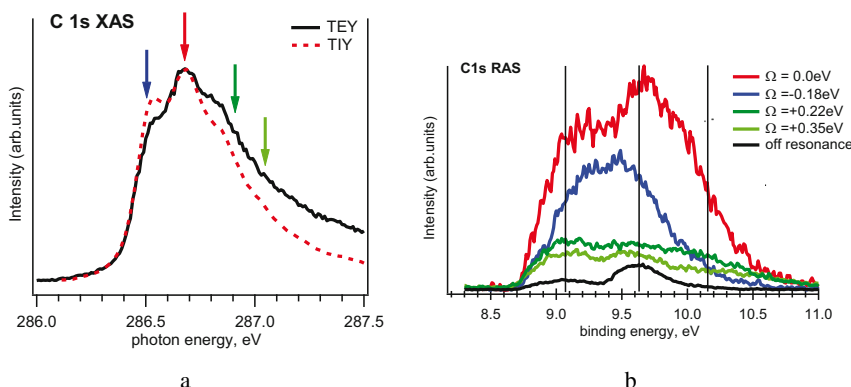


Figure 7.22: (a): X-ray absorption (TIY and TEY) spectra around the C K-edges. The arrows mark the photon energy values at which resonant Auger spectra were recorded. (b): Resonant Auger decay spectra following $C_{2,4}1s \rightarrow \pi_{CO}^*$ excitation at the photon energies marked in Fig. 7.22a. The vertical bars show the positions of the valence orbital ionizations for AcAc ($\pi_{C=C, enol} - 9.08\text{eV}$, $n_O^- - 9.63\text{eV}$ and $n_{O, diketo}^+ - 10.16\text{eV}$ [86]).

In this work we have studied if similar changes in tautomeric equilibrium can be induced by core-hole creation. As was discussed in Chapter 6, the processes related to transient core-excited species occur on a very short timescale, the benchmark of which is set by their intrinsic lifetime of few femtoseconds (~ 7 and ~ 5 fs for $C1s$ and $O1s$ core holes, respectively). Moreover, in addition to the speed of the wave packet propagation, the ability to overcome a reaction barrier would be also crucial in determining whether the isomerization can be feasible in the conditions of the resonant core-electron excitations.

The Auger decay spectra were recorded in the vicinity of the $C1s \rightarrow \pi_{CO}^*$ and $O1s \rightarrow \pi_{CO}^*$ resonances in the binding energy region of 8-12 eV for AcAc in gas phase at room temperature at SPring-8 and MAX II storage rings. The two data sets are basically equivalent, despite the better resolution achievable at SPring-8 and better statistics obtained at MAX-lab at the C K-edge.

The X-ray absorption spectrum of AcAc is shown in Fig. 7.22a and corresponds to the $C1s \rightarrow \pi_{CO}^*$ excitation for carbons with neighboring oxygen atoms (C_2 , C_4 in Fig. 7.20). The Auger decay spectra following $O1s(C_4=O_7) \rightarrow \pi_{CO}^*$ are presented in Fig. 7.23a. All resonant Auger decay spectra, including ‘off resonance’ ones, were normalized to the photon flux, pressure and the number of scans.

From Fig. 7.22b and 7.23 we can see a considerable enhancement of intensity for the final state with a valence electron hole in the $\pi_{C=C, enol}$ orbital at the C K-edge, while at the O K-edge mainly only oxygen lone pairs at 9.63 eV are resonating. This can be understood by the localization of $\pi_{C=C}$ and n_O^- molecular orbitals around the carbon-carbon double bond and mainly on the oxygen ($C=O$), respectively, and therefore a very small overlap between the core-hole intermediate $O1s^{-1}\pi_{CO}^*$ and the cationic final $O1s^2\pi_{C=C}^{-1}$ states.

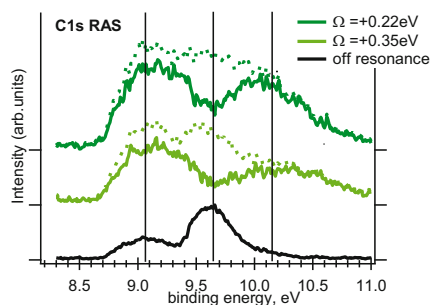


Figure 7.24: Resonant Auger decay spectra for the positive detuning from the $C_{2,4}1s \rightarrow \pi_{CO}^*$ resonance. Dotted lines represent the raw spectra and solid lines the difference with the 'off resonance' spectrum. The vertical bars show the positions of the valence orbital ionizations for AcAc ($\pi_{C=C,enol} - 9.08\text{eV}$, $n_{O^-} - 9.63\text{eV}$ and $n_{O^+,diketo} - 10.16\text{eV}$ [86])

Long vibrational progression in the detuned spectra of $O1s$ decays hampers to perform any additional analysis of the O K-edge deexcitation spectra of AcAc.

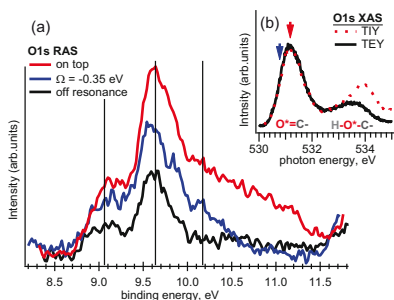


Figure 7.23: (a) Resonant Auger decay spectra recorded on top of the $O_{71}1s \rightarrow \pi_{CO}^*$ resonance and detuned spectrum. The vertical bars show the positions of the valence $\pi_{C=C,enol}$, n_{O^-} and $n_{O^+,diketo}$ orbital ionizations for AcAc. (b) X-ray absorption (TIY and TEY) spectra around the O K-edges ($O1s \rightarrow \pi_{CO}^*$ excitation). The arrows mark the photon energy values at which resonant Auger spectra were recorded.

Positive detuning at the C K-edge (Fig. 7.22b) causes drastic changes to the shape of the Auger decay spectra following $C_{2,4}1s \rightarrow \pi_{CO}^*$ excitation.

Remarkably, in Fig. 7.24 we notice a new peak appearing at 10.16 eV with comparable intensity as for the feature at 9.63 eV, corresponding to oxygen lone pairs in enol. This new spectral feature is exactly at the same binding energy position as the feature corresponding to the n_{O^+} final state in the diketo form [86]. We therefore interpret it as a signature of core-excitation-induced keto-enol tautomerism. An alternative explanation such as Fano-type interference effects of direct and resonant

terms can not cause this kind of dramatic changes in lineshapes of the final states [93]. However, we cannot exclude vibrational excitations. It is known that often by changing the photon energy vibrational distribution in the final state may be also changed. Namely, it apparently may change binding energy as a function of photon energy as a result of the interplay between the potential energy curves of the intermediate and final states. However, larger positive frequency detuning does not cause further shift of the feature around 10.16 eV but rather a decrease of its intensity (Fig. 7.24). This could be an indication of an additional state appearing upon core excitation. Thus we may draw similar-

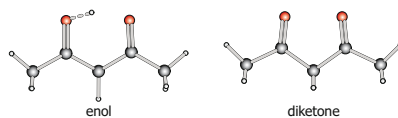


Figure 7.25: Lowest energy isomers of valence ionized acetylacetone.

ities between our experiment and the previous temperature-dependent studies of AcAc [85, 86]. It can be also mentioned that, in contrast to tautomerism of AcAc in the ground state, the geometry of the valence ionized diketone is quite similar to the enol in terms of the co-planar parallel orientation of the C-O bonds (Fig. 7.25). Therefore, large geometrical changes and extensive nuclear motion might not be necessarily required in the intermediate core-excited state to end up in the diketonic final state.

8. Conclusions and Outlook

In this thesis we have performed core-electron spectroscopy studies of molecular systems starting with smaller diatomic, continuing with triatomic and extending our research to more complex polyatomic ones. We can subdivide the results presented here into two categories: the first one focusing on electronic fine structure and effect of the chemical bonds on molecular core levels and the other one dealing with nuclear dynamics induced by creation of a core hole.

Despite the very high resolution achievable nowadays at modern synchrotron radiation sources, interpretation of spectroscopically observed information is frequently difficult due to substantial overlap of spectral features. This can be the case even for simple diatomic molecules, such as Cl_2 studied in the first part of the thesis. However, the combined use of high-resolution spectroscopy with *ab initio* calculations can shed light on the origin of the observed spectroscopic structures and disentangle their complex profiles. This approach enabled us to determine the values of small splittings and differences in the lifetimes for core-hole $2p$ sublevels of Cl_2 which are caused by the presence of the chemical bond.

The effect of the electron density distribution on electronic and nuclear relaxation dynamics after core-electron excitations to LUMO orbitals has been investigated as an example for the N_2O molecule. We have shown that contribution in terms of the Mulliken population of valence molecular orbitals is a determining factor for resonant enhancement of different final states and fragmentation patterns reached after resonant Auger decay.

We have also performed a systematic study of the dependence of the $\text{Cl}1s$ resonant Auger kinetic energies on the presence of different substituents in CH_3X compounds. The observed correlations with substituent constants, which are frequently applied in chemistry for tuning of desired properties in molecules, appear to be surprisingly good. This is at first unexpected due to delocalized nature of the valence molecular orbitals involved in the $\text{Cl}1s \rightarrow \sigma^*$ resonant Auger decay process. However, these correlations may be well described by a model with the “ $Z+1$ ” approximation developed in the presented research.

In the last part of the thesis, where larger polyatomic molecules were studied, our focus was on the spectral features and lineshapes, which may be attributed to the processes, such as nuclear motion, occurring at the same timescale as the core-hole lifetime of $\text{Cl}1s^{-1}\pi^{*1}$ excited states. We were able to identify the main contributions in the X-ray absorption spectrum of allene

on the basis of experimental analysis and confirmed our interpretation by theoretical calculations.

Finally, for the first time we have studied possible isomerization reaction induced by core excitation of acetylacetone. We could observe a new spectral feature in the resonant Auger decay spectra recorded on the high energy side of the $C_{CO}1s \rightarrow \pi^*$ resonance. The energy position of this feature coincides with the position of the final state corresponding to the diketonic tautomer of acetylacetone, which is not observed in the valence and “off resonance” spectra. We therefore interpreted it as a signature of core-excitation-induced keto-enol tautomerism.

The description of the processes involving nuclear rearrangement in polyatomic molecules involves consideration of multidimensional surfaces and many different pathways. An advanced theoretical support could be of a great help in trying to understand the mechanism of isomerization reactions occurring on such a short timescale of few femtoseconds. Besides that one could think of other experiments with *e.g.* energy selected Auger electron/(multi-)ion coincidence techniques to collect more evidence for occurrence of this phenomenon. However, these coincidence experiments would require both high resolution and statistics to be able to observe differences in fragmentation patterns for resonant decays with abundant fragmentation schemes and rearrangements happening during relatively long flight times of fragment ions until they are detected. Kinetic energy releases of different fragment ions and/or photoion-photoion coincidence maps could aid in getting insights into this type of complex processes.

The next step in the line of ultrafast nuclear dynamics happening in transient core-excited species would be the investigation of second-order chemical reactions. A recent considerable progress in cluster science would make accomplishment of two-body reactions induced by synchrotron radiation feasible inside the clusters or on their surfaces. It would open horizons to an unexplored field of core-hole chemistry and modeling of nanoparticles by highly selective site-specific reactions. Here one could also think of utilization of circular polarized light to favor design of species with defined chirality. This could also bring us nearer to check one of the theories on the origin of life and homochirality in biological molecules.

Acknowledgments

First of all, I would like to thank my supervisors – Maria Novella, Svante and Denis – for being a source of knowledge, support and encouragement for me during these years of my PhD studies. I had never imagined that doing PhD in molecular physics could be so much fun and it would not have been possible without you! Not only exploring science has opened its new fascinating and intriguing sides to me. I am also grateful that I was given an opportunity to explore the real world and visit exotic places such as Japan and Brazil for conferences or experiments. I feel lucky that I always could find a wonderful company – you, Denis – to go out during these trips.

I'll extend my gratitude to my colleagues and people I have worked with, especially to Reinhold Fink and Knut Børve who guided me through the winding roads of quantum mechanical calculations. Zhuo whom I have shared office with from the start of my PhD and performed most of the experiments with. I wish you good luck in future and every success after your PhD. Maxim Tchaplyguine who was always helpful and patient over all the phone calls I made to report problems during runs at I411 in MAX-lab. Franz, Georg, Jérôme, Katharina for the pleasure of working with you. Leif Saethre and Knut Børve for the warm welcome and Alf for entertaining me during my visits to Bergen.

I'm cheering my friends and thank them for all the moments of joy spent together. I thank Anja and Edik for supporting me especially in the beginning, when I just arrived in Sweden, and for the master classes in cooking. Andrej and Leonid for infecting me by your passion for downhill-skiing.

I would like to mention my outstanding high school teacher in chemistry, Tatjana Lodeikina, who believed in me first and persuaded me to try myself in chemistry Olympics. I wasn't even close to thinking of studying natural sciences before I met you and I would have made wrong choices without you.

Last but not least, I would like to thank my parents for all the support, warmth and calmness I could always find coming home. Living abroad made me feel more strongly the importance of you in my life not only as parents but as the dearest and wisest friends. I love you and always wanted you to be proud of my deeds!

Appendix

A Summary (in Russian)

Научно-популярное содержание

Всё, что мы видим, едим, вдыхаем, носим или просто используем в своей каждодневной жизни состоит из молекул, которые в свою очередь представляют из себя совокупность атомов всего лишь нескольких дюжин разных сортов. Любой атом, независимо от своей “породы”, - это крохотное ядро и летающие вокруг него малюсенькие электроны. Таким образом, вся обитаемая нами Земля не что иное, как куча из ядер и электронов. Просто удивительно, как они находят пути организовываться, чтобы быть таким невообразимым количеством материй и веществ, окружающими нас! Одна из задач науки - разгадать эту тайну.

Методы и орудия изучения

Метод изучения законов природы, используемый в представленной работе - спектроскопия, которая изучает взаимодействия материй с энергией. Что такое взаимодействие материи с энергией? На самом деле, сами того не подозревая, мы сталкиваемся с этим каждый день: языки пламени от потрескивающих дров в камине, согревающего в зимнюю стужу, или горячий песок на залитом солнцем пляже, или радуга в небе, или же горячая еда из микроволновой печи - всё это незначительная часть примеров подобных взаимодействий. Понятие энергии связывает воедино все явления природы. Например, энергия Солнца передаётся нам в виде света, который раскладывается на составные части, или спектр, включающий инфракрасное, видимое и ультрафиолетовое излучение. Это электромагнитное излучение, которое характеризует определённая длина волны, и чем она короче, тем большей энергией будет обладать это излучение. Например, длина волны красного цвета - 700 нм, а диапазон ультрафиолета - от 100 до 400 нм. 1 нанометр (нм) - это 1 миллионная часть сантиметра. Для сравнения, в микроволновых печах обычно используется длина волн около 12 см, или 12 миллионов нанометров. Энергия с

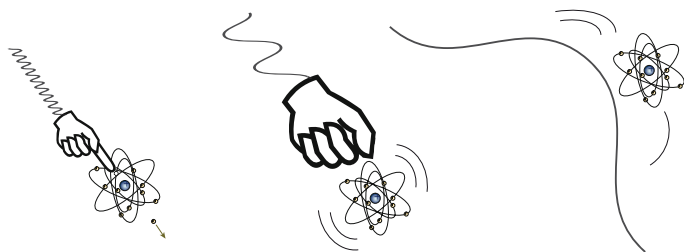


Figure 1: Влияние электромагнитных волн разной длины на атомы.

такой длиной волны заставляет молекулы воды вращаться, при этом тереться друг о друга и от этого нагреваться. Если мы используем 100-нанометровое ультрафиолетовое излучение, то сможем “вытолкнуть” наружу электрон, находящийся у самой поверхности молекулы воды. Чтобы проникнуть дальше вглубь молекулы, нам нужны ещё более короткие волны, а значит и большие энергии излучения. Так, для того чтобы “достать” самый близкий к центру молекулы воды электрон, необходим свет с длиной волны около 2 нм, что соответствует мягкому рентгеновскому излучению. (смотри картинку)

В этой работе мы занимаемся изучением электронов, расположенных близко к ядрам атомов. Поэтому мы используем рентгеновский свет, производимый синхротронами. Синхротрон - это огромная машина от 30 до 800 м в диаметре, внутри которой со скоростью света летают по окружности электроны, при этом, каждый раз поворачивая, электроны излучают свет. Такое излучение встречается и в природе, а именно в космосе, и наблюдается в галактике M87. Мы можем “корректировать” движение электронов в синхротроне и тем самым получать излучение, желаемой энергии и довольно точно соответствующее нашим требованиям, то есть электронным уровням в различных атомах.

Предмет изучения, или что общего у электронов с пчёлами?

Как уже упоминалось, атом состоит из ядра и вращающихся вокруг него малюсеньких электронов. Электроны в атомах не летают как попало, а точно следуют установленному природой множеству законов.

Как, например, и в ульях пчёлы никогда не сидят без дела, а всё время выполняют определённую работу, указанную им уставом высокоорганизованной пчелиной семьи. Они не мешают друг другу, а действуют сообща ради существования своей семьи. Одни пчёлы в силу своей должности (например, пчёлы-уборщики, няньки, корми-

лицы) никогда не покидают улей, другие проводят дни за пределами своего дома в сборе нектара, пыльцы, воды, летая по всей пасеке и встречаясь порой со своими соседями и с нами. Если освобождается вакансия её непременно должна занять другая пчела, чтобы не происходило сбоев в работе улья как единого целого.

Так же и в атомах. Одни электроны находятся во внешних слоях атома. Они принимают участие в образовании связей с другими атомами в молекуле, распространяются по всей молекуле и летают вокруг соседних атомов. Другие электроны обитают вблизи ядра и никогда не покидают свой “дом”-атом.

Ядро атома мы можем сравнить с рамками в улье - чем больше рамок (протонов в ядре), тем больше пчёл (электронов) в улье (атоме). Только электроны (назовём их “электронными пчёлами”) не сидят на ядре и протоны (рамки) вместе с нейтронами, составляющие ядро, находятся все вместе - в центре атома. К тому же в “электронном улье” на каждую “рамку” приходится только по одной “электронной пчеле”, то есть каждому протону соответствует один электрон, а не 2500 пчёл, как в настоящих ульях. Тогда, если мы уберём одну постоянно проживающую в “электронном улье” “электронную пчелу”, то летающие вокруг “улья” “электронные пчёлы” не различают, убавилось ли в доме “электронных пчёл” на одну или стало на одну “рамку” больше. И в том и другом случае, они бурно реагируют на изменения, пытаясь вернуть прежнюю стабильность.

Как уже говорилось, в этой работе мы изучаем “электронные пчёлы”, находящиеся вблизи ядра, то есть “не покидающие свой домик”. Мы их выкидываем из улья-атома за пределы пасеки-молекулы или выводим к другим “электронным пчёлам”, летающим вокруг всех “ульев”. Что при этом происходит на “электронной пасеке”(т.е. в молекуле)? Распадутся ли или трансформируются пчелиные семьи? Кто займёт освободившуюся вакансию? Как это произойдёт? И сколько времени на это уйдёт? Ответы на эти вопросы позволяют нам определить также и прежнюю роль и влияние “электронной пчелы”, выкинутой нами из домика-атома.

Разные породы пчёл на пасеках ведут себя по-разному. Некоторые виды пчелиных семей любят воровать из соседних ульев, в то время как другие бывают агрессивные и жёстко охраняют свои дома от любого вторжения, а третьи слишком слабые, чтобы выдерживать какую-либо разбойную атаку. Так же и разные виды атомов или групп атомов: одни пытаются перетянуть на себя соседние электроны, другие ни за что их не отдадут, а третьи охотно делятся ими сами (в отличие от атомов, пчёлы никогда охотно ничего не отдают). Какое влияние это оказывает на “электронных пчёл”, не покидающих свой домик, тоже исследуется в данной диссертации.

Так же, как необходимо изучать и понимать принципы и устройство пчелиных семей, чтобы впоследствии, применяя приобретённые знания, получать более качественный и вкусный мёд и другие продукты пчеловодства в больших объёмах, так и важно исследовать строения и свойства атомов, чтобы можно было составлять молекулы с различными характеристиками и моделировать новые материалы с улучшенными качествами, включая, например, более эффективные и безвредные лекарственные препараты или материалы с гигантским магнитным сопротивлением, открытие которых было удостоено Нобелевской премии в прошлом году и позволило уменьшить размеры жёстких дисков и в то же время увеличить их вместимость.

Bibliography

- [1] Siegbahn, K., Nordling, C., Johansson, G., Hedman, J., Heden, P. F., Hamrin, K., Gelius, U., Bergmark, T., Werme, L. O., Manne, R., and Baer, Y. *ESCA applied to free molecules*. North-Holland, Amsterdam, (1969).
- [2] Service, R. F. *Science* **298**(15), 1356 (2002).
- [3] Attwood, D. *Soft x-rays and extreme ultraviolet radiation. Principles and applications*. CUP, (1999).
- [4] Bässler, M., Ausmees, A., Jurvansuu, M., Feifel, R., Forsell, J.-O., de Tarso Fonseca, P., Kivimäki, A., Sundin, S., Sorensen, S. L., Nyholm, R., Björneholm, O., Aksela, S., and Svensson, S. *Nucl. Instrum. Methods A* **469**, 382 (2001).
- [5] Nyholm, R., Svensson, S., Nordgren, J., and Flodström, A. *Nucl. Instrum. Methods A* **246**, 267 May (1986).
- [6] Mårtensson, N., Baltzer, P., Brühwiler, P. A., Forsell, J.-O., Nilsson, A., Stenborg, A., and Wannberg, B. *J. Electron Spectrosc. Relat. Phenom.* **70**, 117 (1994).
- [7] Ohashi, H., Ishiguro, E., Tamenori, Y., Kishimoto, H., Tanaka, M., Irie, M., Tanaka, T., and Ishikawa, T. *Nucl. Instr. Methods A* **486-487**, 529 (2001).
- [8] Tanaka, T. and Kitamura, H. *J. Synchrotron Rad.* **3**, 47 (1996).
- [9] Ohashi, H., Ishiguro, E., Tamenori, Y., Okumura, H., Hiraya, A., Yoshida, H., Senba, Y., Okada, K., Saito, N., and Suzuki, I. H. e. a. *Nucl. Instr. Methods A* **486-487**, 533 (2001).
- [10] Shimizu, Y., Ohashi, H., Tamenori, Y., Muramatsu, Y., Yoshida, H., Okada, K., Saito, N., Tanaka, H., Koyano, I., Shin, S., and Ueda, K. **114-116**, 63 (2001).
- [11] Prümper, G., Ueda, K., Hergenhahn, U., De Fanis, A., Tamenori, Y., Kitajima, M., Hoshino, M., and Tanaka, H. *J. Electron Spectrosc. Relat. Phenom.* **144-147**, 227 (2005).

- [12] Prümper, G., Tamenori, Y., Fanis, A. D., Hergenbahn, U., Kitajima, M., Hoshino, M., Tanaka, H., and Ueda, K. *J. Phys. B* **38**, 1 (2005).
- [13] Hertz, H. *Ann. Phys. Chem.* **31**, 983 (1887).
- [14] Einstein, A. *Ann. Physik* **17**, 132 (1905).
- [15] Simon, M., Lebrun, T., Martins, R., de Souza, G. G. B., Nenner, I., Lavollee, M., and Morin, P. *J. Phys. Chem.* **97**, 5228 (1993).
- [16] Schmelz, H. C., Reynaud, C., Simon, M., and Nenner, I. *J. Chem. Phys.* **101**, 3742 (1994).
- [17] Miron, C., Simon, M., Leclercq, N., Hansen, D. L., and Morin, P. *Phys. Rev. Lett.* **81**, 4104 (1998).
- [18] Céolin, D., Miron, C., Guen, K. L., Guillemin, R., Morin, P., Shigemasa, E., Millié, P., Ahmad, M., Lablanquie, P., Penent, F., and Simon, M. *J. Chem. Phys.* **123**, 234303 (2005).
- [19] Atkins, P. and Friedman, R. *Molecular Quantum Mechanics*. OUP, 3rd edition, (1999).
- [20] Gelius, U., Svensson, S., Siegbahn, H., Basilier, E., Faxälv, Å., and Siegbahn, K. *Chem. Phys. Lett.* **28**, 1 (1974).
- [21] Kukk, E., Ueda, K., Hergenbahn, U., Liu, X., Prumper, G., Yoshida, H., Tamenori, Y., Makochekanwa, C., Tanaka, T., Kitajima, M., and Tanaka, H. *Phys. Rev. Lett.* **95**, 133001 (2005).
- [22] Cutler, J., Bancroft, G., Sutherland, D., and Tan, K. *Phys. Rev. Lett.* **67**, 1531 (1991).
- [23] Svensson, S., Ausmees, A., Osborne, S. J., Bray, G., Gel'mukhanov, F., Ågren, H., Naves de Brito, A., Sairanen, O.-P., Nömmiste, E., Aksela, H., and Aksela, S. *Phys. Rev. Lett.* **72**, 3021 (1994).
- [24] Svensson, S., Naves de Brito, A., Keane, M. P., and Karlsson, L. *Phys. Rev. A* **43**, 6441 (1991).
- [25] Fink, R. F., Kivilompolo, M., Aksela, H., and Aksela, S. *Phys. Rev. A* **58**, 1988 (1998).
- [26] Svensson, S., Aksela, H., and Aksela, S. *J. Electron Spectrosc. Relat. Phenom.* **75**, 67 (1995).
- [27] Kivilompolo, M., Kivimäki, A., Jurvansuu, M., Aksela, H., Aksela, S., and Fink, R. F. *J. Phys. B.* **33**, L157 (2000).
- [28] Gel'mukhanov, F., Ågren, H., Svensson, S., Aksela, H., and Aksela, S. *Phys. Rev. A* **53**, 1379 (1996).

-
- [29] Bueno, A. M., de Brito, A. N., Fink, R. F., Bässler, M., Björneholm, O., Burmeister, F., Feifel, R., Miron, C., Sorensen, S. L., Wang, H., and Svensson, S. *Phys. Rev. A* **67**, 022714 (2003).
- [30] Liu, Z. F., Bancroft, G. M., Tan, K. H., and Schachter, M. *J. Electron Spectrosc. Relat. Phenom.* **67**, 299 (1994).
- [31] Matila, T., Püttner, R., Kivimäki, A., Aksela, H., and Aksela, S. *J. Phys. B* **35**(22), 4607–4611 (2002).
- [32] Kempgens, B., Köppel, H., Kivimäki, A., Neeb, M., Cederbaum, L. S., and Bradshaw, A. M. *Phys. Rev. Lett.* **79**, 3617 (1997).
- [33] Thomas, T., Berrah, N., Bozek, J., Carrol, T., Hahne, J., Karlsen, T., Kuk, E., and Saethre, L. *Phys. Rev. Lett.* **82**, 1120 (1999).
- [34] Hergenbahn, U., Kugeler, O., Rüdél, A., Rennie, E., and Bradshaw, A. *J. Phys. Chem. A* **105**, 5704 (2001).
- [35] Kosugi, N. *Chem. Phys.* **289**, 117 (2003).
- [36] Kosugi, N. *J. Electron Spectrosc. Relat. Phenom.* **137-140**, 335 (2004).
- [37] Kuk, E. Curve fitting macro package SPANCF. <http://www.geocities.com/ekukk>.
- [38] Colbert, D. T. and Miller, W. H. *J. Chem. Phys.* **96**, 1982 (1992).
- [39] Van der Straten, P., Morgenstern, R., and Niehaus, A. *Z. Phys. D* **8**, 35 (1988).
- [40] Nummert, V., Travnikova, O., Vahur, S., Leito, I., Piirsalu, M., Mäemets, V., Koppel, I., and Koppel, I. A. *J. Phys. Org. Chem.* **19**, 654 (2006).
- [41] Pratt, D., DiLabio, G., Mulder, P., and Ingold, K. *Acc. Chem. Res.* **37**, 334 (2004).
- [42] Exner, O. and Böhm, S. *Curr. Org. Chem.* **10**, 763 (2006).
- [43] Žáček, P., Dransfeld, A., Exner, O., and Schraml, J. *Magn. Reson. Chem.* **44**, 1073 (2006).
- [44] Cauletti, C., Giancaspro, C., Monaci, A., and Piancastelli, M. N. *J. Chem. Soc., Perkin Trans. 2*, 656 (1981).
- [45] Taft, R. W. *Steric Effects in Organic Molecules*. Wiley, New York, (1956).
- [46] McNaught, A. D. and Wilkinson, A. *Compendium of Chemical Terminology The Gold Book*. Blackwell Science, Oxford, 2nd edition, (1997).
- [47] Taft, R. W. and Topsom, R. D. *Prog. Phys. Org. Chem.* **61**, 1 (1987).

- [48] Exner, O. and Böhm, S. *J. Phys. Org. Chem.* **19**, 393 (2006).
- [49] Čársky, P., Nauš, P., and Exner, O. *J. Phys. Org. Chem.* **11**, 485 (1998).
- [50] Exner, O. and Böhm, S. *Eur. J. Org. Chem.* **2007**, 2870 (2007).
- [51] Lindberg, B., Svensson, S., Malmquist, P. A., Basilier, E., Gelius, U., and Siegbahn, K. *Chem. Phys. Lett.* **40**, 175 (1976).
- [52] Sacher, E. *Appl. Surf. Sci.* **74**, 129 (1994).
- [53] Myrseth, V., Saethre, L., Børve, K., and Thomas, T. *J. Org. Chem.* **72**, 5715 (2007).
- [54] Thomas, T., Saethre, L., Børve, K., Bozek, J., Huttula, M., and Kukk, E. *J. Phys. Chem. A* **108**, 4983 (2004).
- [55] Björneholm, O., Sundin, S., Svensson, S., Marinho, R. R. T., Naves de Brito, A., Gel'mukhanov, F., and Ågren, H. *Phys. Rev. Lett.* **79**, 3150 (1997).
- [56] Baev, A., Salek, P., Gel'mukhanov, F., Ågren, H., Naves de Brito, A., Björneholm, O., and Svensson, S. *Chem. Phys.* **289**, 51 (2003).
- [57] Salek, P., Baev, A., Gel'mukhanov, F., and Ågren, H. *Phys. Chem. Chem. Phys.* **5**, 1 (2003).
- [58] Skytt, P., Glans, P., Guo, J.-H., Gunnelin, K., Sâthe, C., Nordgren, J., Gel'mukhanov, F. Kh., Cesar, A., and Ågren, H. *Phys. Rev. Lett.* **77**, 5035 (1996).
- [59] Morin, P. and Nenner, I. *Phys. Rev. Lett.* **56**, 1913 (1986).
- [60] Aksela, H., Aksela, S., Ala-Korpela, M., Sairanen, O.-P., Hotokka, M., Bancroft, G. M., Tan, K. H., and Tulkki, J. *Phys. Rev. A* **41**, 6000 (1990).
- [61] Aksela, H., Aksela, S., Naves de Brito, A., Bancroft, G. M., and Tan, K. H. *Phys. Rev. A* **45**, 7948 (1992).
- [62] Guen, K. L., Miron, C., Céolin, D., Guillemin, R., Leclercq, N., Simon, M., Morin, P., Mocellin, A., Björneholm, O., de Brito, A. N., and Sorensen, S. L. *J. Chem. Phys.* **127**, 114315 (2007).
- [63] Hjelte, I., Piancastelli, M. N., Fink, R. F., Björneholm, O., Bässler, M., Feifel, R., Giertz, A., Wang, H., Wiesner, K., Ausmees, A., Miron, C., Sorensen, S. L., and Svensson, S. *Chem. Phys. Lett.* **334**, 151 (2001).
- [64] Hjelte, I., Piancastelli, M. N., Jansson, C. M., Wiesner, K., Björneholm, O., Bässler, M., Sorensen, S. L., and Svensson, S. *Chem. Phys. Lett.* **370**, 781 (2003).

-
- [65] Salek, P., Carravetta, V., Gel'mukhanov, F. K., Ågren, H., Schimmelpfennig, B., Piancastelli, M. N., Sorensen, L., Feifel, R., Hjelte, I., Bässler, M., Svensson, S., Björneholm, O., and Naves de Brito, A. *Chem. Phys. Lett.* (2001).
- [66] Schaphorst, S. J., Caldwell, C. D., Krause, M. O., and Jiménez-Mier, J. *Chem. Phys. Lett.* **213**, 315 (1993).
- [67] Naves de Brito, A., Hjelte, I., Wiesner, K., Feifel, R., Bässler, M., Sorensen, S. L., Björneholm, O., Piancastelli, M. N., Karlsson, L., and Svensson, S. *Phys. Rev. A* **64**, 054702 (2001).
- [68] Gel'mukhanov, F. and Ågren, H. *Phys. Rev. A* **54**, 379 (1996).
- [69] Miron, C., Simon, M., Morin, P., Nanbu, S., Kosugi, N., Sorensen, S. L., de Brito, A. N., Piancastelli, M. N., Björneholm, O., Feifel, R., Bässler, M., and Svensson, S. *J. Chem. Phys.* **115**, 864 (2001).
- [70] Fink, R. F., Kivilompolo, M., and Aksela, H. *J. Chem. Phys.* **111**, 10034 (1999).
- [71] Ehara, M., Tamaki, R., Nakatsuji, H., Lucchese, R., Söderström, J., Tanaka, T., Hoshino, M., Kitajima, M., Tanaka, H., De Fanis, A., and Ueda, K. *Chem. Phys. Lett.* **438**, 14 (2007).
- [72] Alagia, M., Richter, R., Stranges, S., Agaker, M., Strom, M., Soderstrom, J., Sathe, C., Feifel, R., Sorensen, S., Fanis, A. D., Ueda, K., Fink, R., and Rubensson, J.-E. *Phys. Rev. A* **71**, 012506 (2005).
- [73] Adachi, J.-I., Kosugi, N., Shigemasa, E., and Yagishita, A. *J. Chem. Phys.* **102**, 7369 (1995).
- [74] Tanaka, T., Shindo, H., Makochekanwa, C., Kitajima, M., Tanaka, H., Fanis, A. D., Tamenori, Y., Okada, K., Feifel, R., Sorensen, S., Kuk, E., and Ueda, K. *Phys. Rev. A* **72**, 022507 (2005).
- [75] Larkins, F. P. *J. Chem. Phys.* **86**, 3239 (1987).
- [76] Kimura, K., Katsumata, S., Achiba, Y., Yamaxaki, T., and Iwata, S. *Handbook of HeI Photoelectron Spectra of Fundamental Organic Molecules*. Halsted Press, New York, (1981).
- [77] Piancastelli, M. N., Neeb, M., Kivimäki, A., Kempgens, B., Köppe, H. M., Maier, K., Bradshaw, A. M., and Fink, R. F. *J. Phys. B* **30**, 5677 (1997).
- [78] Ehara, M., Yasuda, S., and Nakatsuji, H. *Z. Phys. Chem.* **217**, 161 (2003).
- [79] Kinmond, E., Eland, J. H. D., and Karlsson, L. *Int. Journal of Mass Spectrom.* **185-187**, 437 (1999).

- [80] Baltzer, P., Wannberg, B., Lundqvist, M., Karlsson, L., Holland, D. M. P., MacDonald, M. A., and von Niessen, W. *Chem. Phys.* **196**, 551 (1995).
- [81] Yang, Z. Z., Wang, L. S., Lee, Y. T., Shirley, D. A., Huang, S. Y., and Lester, W. A. *Chem. Phys. Lett.* **171**, 9 (1990).
- [82] Cederbaum, L. S., Domcke, W., and Köppel, H. *Chem. Phys.* **33**, 319 (1978).
- [83] Woywod, C. and Domcke, W. *Chem. Phys.* **162**, 349 (1992).
- [84] Karlsen, T. and Børve, K. J. *J. Chem. Phys.* **112**, 7979 (2000).
- [85] Schweig, A., Vermeer, H., and Weidner, U. *Chem. Phys. Lett.* **26**, 229 (1974).
- [86] Hush, N. S., Livett, M. K., Peel, J. B., and Willett, G. D. *Aust. J. Chem.* **40**, 599 (1987).
- [87] Chen, X.-B., Fang, W.-H., and Phillips, D. *J. Phys. Chem. A* **110**, 4434 (2006).
- [88] Brown, R. S. *J. Am. Chem. Soc.* **99**, 5497 (1977).
- [89] Brown, R. S., Tse, A., Nakashima, T., and Haddon, R. C. *J. Am. Chem. Soc.* **101**, 3157 (1979).
- [90] Clark, D. T. and Harrison, A. *J. Electron Spectrosc. Relat. Phenom.* **23**, 39 (1981).
- [91] Broadbent, S. A., Burns, L. A., Chatterjee, C., and Vaccaro, P. H. *Chem. Phys. Lett.* **434**, 31 (2007).
- [92] Temprado, M., Roux, M., Umnahanant, P., Zhao, H., and Chickos, J. *J. Phys. Chem. B* **109**, 12590 (2005).
- [93] Carravetta, V., F. Kh. Gel'mukhanov, Ågren, H., Sundin, S., Osborne, S. J., Naves de Brito, A., Björneholm, O., Ausmees, A., and Svensson, S. *Phys. Rev. A* **56**, 4665 (1997).

Acta Universitatis Upsaliensis

*Digital Comprehensive Summaries of Uppsala Dissertations
from the Faculty of Science and Technology 442*

Editor: The Dean of the Faculty of Science and Technology

A doctoral dissertation from the Faculty of Science and Technology, Uppsala University, is usually a summary of a number of papers. A few copies of the complete dissertation are kept at major Swedish research libraries, while the summary alone is distributed internationally through the series Digital Comprehensive Summaries of Uppsala Dissertations from the Faculty of Science and Technology. (Prior to January, 2005, the series was published under the title "Comprehensive Summaries of Uppsala Dissertations from the Faculty of Science and Technology".)



ACTA
UNIVERSITATIS
UPSALIENSIS
UPPSALA
2008

Distribution: publications.uu.se
urn:nbn:se:uu:diva-8904